ARTICLES
https://doi.org/10.1038/s41590-021-01013-0

nature immunology

Effector differentiation downstream of lineage commitment in ILC1s is driven by Hobit across tissues

Christin Friedrich[1,10], Renske L. R. E. Taggenbrock[2,10], Rémi Doucet-Ladevèze[1], Gosia Golda[3,4,5], Rebekka Moenius[1], Panagiota Arampatzi[6], Natasja A. M. Kragten[2], Katharina Kreymborg[7], Mercedes Gomez de Agüero[1], Wolfgang Kastenmüller[1], Antoine-Emmanuel Saliba[8], Dominic Grün[1,3], Klaas P. J. M. van Gisbergen[2,9,11] and Georg Gasteiger[1,11] ✉

Innate lymphoid cells (ILCs) participate in tissue homeostasis, inflammation, and early immunity against infection. It is unclear how ILCs acquire effector function and whether these mechanisms differ between organs. Through multiplexed single-cell mRNA sequencing, we identified cKit^{+}CD127^{hi}TCF-1^{hi} early differentiation stages of T-bet^{+} ILC1s. These cells were present across different organs and had the potential to mature toward CD127^{int}TCF-1^{int} and CD127^{-}TCF-1^{-} ILC1s. Paralleling a gradual loss of TCF-1, differentiating ILC1s forfeited their expansion potential while increasing expression of effector molecules, reminiscent of T cell differentiation in secondary lymphoid organs. The transcription factor Hobit was induced in TCF-1^{hi} ILC1s and was required for their effector differentiation. These findings reveal sequential mechanisms of ILC1 lineage commitment and effector differentiation that are conserved across tissues. Our analyses suggest that ILC1s emerge as TCF-1^{hi} cells in the periphery and acquire a spectrum of organ-specific effector phenotypes through a uniform Hobit-dependent differentiation pathway driven by local cues.

Nonlymphoid organs are populated by innate lymphoid cells (ILCs) that initiate rapid local immune responses, regulate tissue homeostasis, and contribute to inflammatory diseases. As tissue-resident cells, ILCs adapt to their environment and exhibit a spectrum of organ-specific phenotypes and functions[1–3]. We and others have recently identified tissue-associated ILC progenitors (ILCPs) that exhibit multilineage potential, supporting the concept that ILCs can develop and mature within adult tissues[4–6]. ILCPs gain expression of master transcription factors that determine the lineage choice of developing ILCs and enable the acquisition of prototypic effector functions that direct immunity against viruses, bacteria, or parasites[1,2]. The specification of ILC1, ILC2, and ILC3 through lineage-defining transcription factors T-bet, Gata-3, and Rorγt, respectively, parallels the polarization of antigen-experienced T cells. A key feature of T cell immunity is the compartmentalization of polarized cells into memory- and effector-like cells, which represent early versus more terminal differentiation stages, respectively, and which are characterized by distinct capacities for re-expansion and immediate expression of effector molecules. Whether and how ILCs undergo further effector differentiation beyond the stage of lineage commitment is currently unclear[3,7]. Major open questions are how ILC heterogeneity and effector specialization are established, how these processes are transcriptionally regulated, and whether underlying pathways are conserved across organs[3,7–10]. Understanding the mechanisms regulating the effector function of ILCs is of special importance owing to their broad functions in tissue immunity, tissue homeostasis, and inflammatory diseases.

Here, we addressed these questions for ILC1s, which exhibit pronounced tissue-specific heterogeneity. We report the identification of distinct maturation stages of ILC1s that are developmentally related along a differentiation trajectory, on which cells gradually decreased their proliferative potential in response to homeostatic cytokines, while gaining expression of effector molecules. We identified TCF-1^{hi} early maturation stages of ILC1s that already expressed the lineage-defining transcription factor T-bet, but shared gene-expression patterns with ILC progenitors. These CD127^{hi}TCF-1^{hi} 'early' ILC1s, which were present across different organs, initiated expression of the transcription factor Hobit to drive their stepwise differentiation into downstream CD127^{int}TCF-1^{int} and CD127^{-}TCF-1^{-} effector cells. These findings reveal sequential mechanisms of ILC1 lineage commitment and ILC1 effector maturation and highlight remarkable similarities between the population structure and effector maturation of

[1]Würzburg Institute of Systems Immunology (WüSI), Max Planck Research Group at the Julius-Maximilians-Universität Würzburg, Würzburg, Germany. [2]Department of Hematopoiesis, Sanquin Research and Landsteiner Laboratory, Amsterdam UMC, University of Amsterdam, Amsterdam, the Netherlands. [3]Max Planck Institute of Immunobiology and Epigenetics, Freiburg, Germany. [4]Faculty of Biology, University of Freiburg, Freiburg, Germany. [5]International Max Planck Research School for Immunology, Epigenetics and Metabolism (IMPRS-IEM), Freiburg, Germany. [6]Core Unit Systems Medicine, Julius-Maximilians-Universität Würzburg, Würzburg, Germany. [7]Roche Innovation Center Munich, Oncology Division, Roche Pharmaceutical Research and Early Development, Penzberg, Germany. [8]Helmholtz Institute for RNA-based Infection Research (HIRI), Helmholtz-Center for Infection Research (HZI), Würzburg, Germany. [9]Department of Experimental Immunology, Amsterdam UMC, University of Amsterdam, Amsterdam, the Netherlands. [10]These authors contributed equally: Christin Friedrich, Renske L. R. E. Taggenbrock. [11]These authors jointly supervised this work: Klaas P. J. M. van Gisbergen, Georg Gasteiger. ✉e-mail: georg.gasteiger@uni-wuerzburg.de

ILCs and antigen-experienced T cells. Our analyses suggest that effector differentiation of committed ILC1s is established through a uniform Hobit-dependent pathway in ILC1 populations across peripheral tissues.

Results

CD127 identifies helper- and cytotoxic-like hepatic ILC1s. Hepatic ILC1s are Lin$^-$NK1.1$^+$Eomes$^-$ cells characterized by expression of CD49a, Cxcr6, TRAIL, and CD200r[11–15]. We could identify these cells through a fluorescent reporter of the transcription factor Hobit, which is required for the generation of hepatic ILC1s[16,17] (Fig. 1a,b and Extended Data Fig. 1a). Within the ILC lineages, expression of Hobit was specifically detected in ILC1s, as described[16,18], but not in natural killer (NK) cells (Fig. 1b). To characterize hepatic ILC1s in more depth, we sorted Lin$^-$NK1.1$^+$ cells and enriched CD49b$^-$Hobit^{Tom+} ILCs for cellular indexing of transcriptomes and epitopes by sequencing (CITE-seq) (Fig. 1c, Extended Data Fig. 1b,c, and Supplementary Table 1). Our sequencing analysis, which is accessible as an interactive online resource (https://go.uniwue.de/hobit), revealed that hepatic ILC1 comprised two populations that segregated through the expression of *Il7r* transcript and its corresponding protein CD127 (Fig. 1c,d). CD127$^+$ and CD127$^-$ ILC1s expressed comparable levels of the surface molecules Cxcr6, CD49a, CD200r, and TRAIL, as well as the transcription factors T-bet and Hobit, but lacked expression of CD49b, Eomes, and Rorγt, defining them as bona-fide ILC1s (Fig. 1e and Extended Data Fig. 1d,e). CD127$^+$ ILC1s expressed increased levels of interleukin-18 receptor 1 (IL-18R1) and CD160, whereas CD127$^-$ ILC1s were characterized by preferential expression of the transmembrane protein CD3γ and granzymes A, B, and C (Fig. 1f), consistent with the cytotoxic function of ILCs previously observed in mice and humans[9,14,19–22]. Indeed, while CD127$^+$ had a modestly increased capacity to produce the cytokines interferon-γ (IFN-γ), tumor necrosis factor (TNF), and granulocyte-macrophage colony-stimulating factor (GM-CSF), CD127$^-$ ILC1s were able to kill YAC target cells more efficiently than were their CD127$^+$ counterparts (Fig. 1g,h). These analyses revealed that CD127$^+$ and CD127$^-$ hepatic ILC1s represent distinct populations with gene-expression patterns reminiscent of helper-like and cytotoxic-like cells.

CD127$^-$ cytotoxic-like cells are bona-fide ILC1s. CD127$^-$ cytotoxic-like cells clustered with canonical CD127$^+$ ILC1s and not with Eomes$^+$ conventional NK (cNK) cells (Fig. 1c), and expressed *Cd200r*, *Cxcr6*, *Tnfsf10*, *Itga1*, *Cd7*, *Il21r*, *Ahr*, *Socs2*, *Inpp4b*, *Ckb*, *Rgs1*, *CD69*, germline-encoded *Tcrg* transcripts, and the cytokine *Xcl1*, all of which are part of a core signature distinguishing liver ILC1s from cNK cells[18], but lacked expression of *Sell*, *Itga4*, *Itgam*, *Itga2*, *S1pr5*, *Cx3cr1*, *Zeb2*, *Cma1*, *Serpinb9b*, and *Irf8*, as well as Ly49 receptors *Klra4*, *Klra7*, and *Klra8*, which are characteristically expressed by cNK cells (Extended Data Fig. 2a). In addition, CD127$^-$ ILC1 developed normally in NKp46^{Cre} Eomes$^{fl/fl}$ mice that are devoid of cNK cells (Extended Data Fig. 2b), as well as in T cell-deficient *Rag1*$^{-/-}$ mice (Extended Data Fig. 2c). Both CD127$^+$ and CD127$^-$ ILC1 subsets, but not cNK cells, exhibited a high degree of fate mapping for *Rorc* expression, which can identify ILC1s that have differentiated from ILC3s[23,24] or from subsets of ILCPs marked by stochastic expression of *Rorc*[4,25]. This fate-mapping analysis suggests that CD127$^+$ and CD127$^-$ ILC1 subsets have a shared developmental origin but are separate from cNK cells. Conversely, both FM$^+$ and FM$^-$ cells showed a similar pattern of CD127, IL-18R1, and granzyme expression (Extended Data Fig. 2d,e). Consistent with the idea that granzyme-expressing ILC1s differentiated as part of a developmental program in the absence of microbial challenges, both helper- and cytotoxic-like ILC1s were readily detected in gnotobiotic (germ-free) mice (Extended Data Fig. 2f). In combination, these phenotypic and developmental similarities suggest that CD127$^+$ and CD127$^-$ ILC populations represent distinct subsets in the ILC1 lineage.

CD127$^+$ ILC1s are precursors of CD127$^-$ cytotoxic-like ILC1s. CD127$^+$ and CD127$^-$ ILC1s shared a core gene-expression program, while many genes, including those encoding cytokine receptors (for example *Il7r* and *Il18r1*) and effector molecules (for example *Fgl2*, *Ccl5*, *S100a6*, *Gzma*, and *Gzmb*) were differentially expressed (Fig. 2a). Reminiscent of the potential for cytokine production and cytotoxicity (Fig. 1g,h), expression of these genes was not mutually exclusive among CD127$^+$ and CD127$^-$ subsets, but instead appeared to be gradually increased in one or the other cluster, raising the possibility that these ILC1 subsets represented extremes of a continuous spectrum of differentiation states. Indeed, pseudotemporal ordering of single-cell transcriptomes suggested that CD127$^+$ ILC1s can differentiate into CD127$^-$ ILC1s by gradually downregulating *Il7r* and *Il18r1* while gaining expression of effector-molecule genes *Gzma, Gzmb*, and *Cd3g* (Fig. 2b). In fact, when cultured on OP9-DL1 feeder cells, CD127$^+$ ILC1s showed vigorous expansion and lost expression of CD127 and IL-18R1 while gaining expression of CD3γ, Gzma, and Gzmb, and hence acquired a phenotype of CD127$^-$IL-18R1$^-$Eomes$^-$CD49a$^+$ cytotoxic-like ILC1s (Fig. 2c–e and Extended Data Fig. 3a–c). This differentiation occurred independently of stimulation with the notch ligand DL1, as similar results were obtained with OP9 and OP9-DL4 feeder cells (Extended Data Fig. 3d). Because IL-2 may activate ILC1s, we tested their differentiation in the presence of IL-15, which is an essential homeostatic cytokine and differentiation factor for ILC1s[11,26]. The overall expansion was substantially reduced in the IL-15- versus IL-2-supplemented cultures, yet CD127$^+$ ILC1s still gave rise to Gzma- and Gzmb-expressing CD127$^-$ cells. Notably, a higher fraction of cells retained their original phenotype (CD127$^+$Gzma$^-$Gzmb$^-$) in the presence of IL-15, consistent with the idea that IL-15 maintains a proportion of ILC1s in an early differentiation state, and reminiscent of homeostatic conditions in vivo (Extended Data Fig. 3e). In contrast to CD127$^+$ ILC1s, CD127$^-$ ILC1s showed an impaired expansion in all experimental conditions that we tested and remained CD127$^-$, whereas CD3γ, Gzma, and Gzmb expression were further increased during culture (Fig. 2c–e and Extended Data Fig. 3c–e). CTV labeling showed that the increased expansion potential of CD127$^+$ ILC1s compared with that of CD127$^-$ ILC1s associated with increased proliferation of this ILC1 subset (Extended Data Fig. 3f). These findings were recapitulated when ILC1 subsets differentiated in vivo after adoptive transfer (Fig. 2f,g and Extended Data Fig. 3g). Of note, CD127$^+$ cells generated significantly more cytotoxic-like ILC1s than did their CD127$^-$ counterparts in vitro and in vivo, highlighting the differentiation and expansion potential of CD127$^+$ ILC1s.

TCF-1^{hi} cells are early differentiation stages of ILC1s. These data established that CD127$^+$ and CD127$^-$ hepatic cells represent a continuous spectrum of cellular differentiation states of ILC1s that are related along a developmental path. The observation that CD127$^+$ ILC1s had a pronounced expansion and differentiation potential prompted us to ask whether early progenitor-like developmental stages of ILC1s were present in the tissue. To address this question, we analyzed our single-cell RNA sequencing (scRNA-seq) dataset with RaceID3, which has improved performance in the identification of relatively rare cell types, and performed subsequent StemID analysis to infer putative lineage relationships (Fig. 3a–c). These analyses identified three clusters of ILC1s, one of which was characterized by increased expression of *Kit* and *Tcf7* (the gene encoding TCF-1), and a high relative transcriptome entropy, a criterion used to identify immature or stem-like populations in scRNA-seq datasets[27]. In addition to *Kit* and *Tcf7*, these cells expressed high levels of *Il7r*, *Il18r1*, *Emb*, *Rora*, *and Ikzf2*, all of

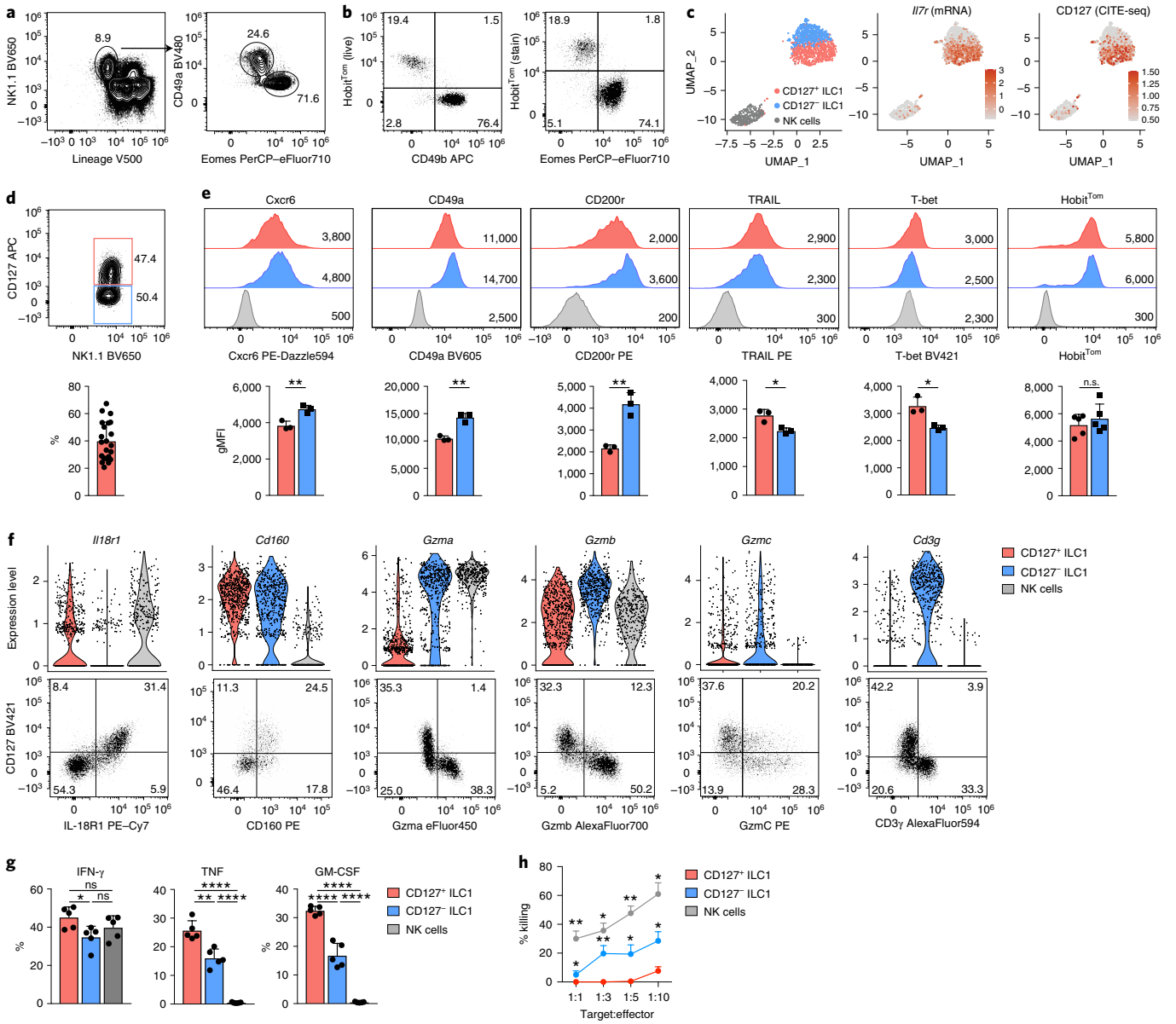

Fig. 1 | Differential expression of CD127 identifies helper-like and cytotoxic-like hepatic ILC1s. a,**b**, Representative FACS analysis showing the gating strategy used to identify liver CD45⁺Lin⁻NK1.1⁺CD49a⁺Eomes⁻ ILC1s (**a**) and tdTomato (Tom) Hobit reporter signal (**b**) in Lin⁻NK1.1⁺ cells in Hobit$^{Tom/WT}$ mice. **c**–**f**, Cellular indexing of transcriptomes and epitopes by sequencing (CITE-seq) of liver ILC1s and NK cells sorted from Hobit$^{Tom/WT}$ mice. **c**, Uniform manifold approximation and projection (UMAP) visualization of 1,545 single-cell transcriptomes delineating liver ILC1 and NK cell clusters identified on the basis of their transcriptional signatures (left) and colored according to the $\log_{10}$-normalized expression of *Il7r* mRNA (middle) and protein (CITE-seq) (right). **d**, Representative FACS analysis of CD127 expression on liver ILC1s. The bar graph shows the frequency of CD127⁺ cells within liver Lin⁻NK1.1⁺Eomes⁻CD49a⁺ ILC1s. Data are pooled from 7 independent experiments with $n = 2$–5 mice (total $n = 22$ mice). **e**, Representative histograms showing expression of indicated markers by CD127⁺ and CD127⁻ liver ILC1s and NK cells of WT and Hobit$^{Tom/WT}$ mice. Bar graphs show the geometric mean of fluorescence intensity (gMFI) of protein and reporter expression. Data are representative of more than 3 individual experiments with $n = 3$ WT mice, or pooled from 2 individual experiments with $n = 2$ and 3 Hobit$^{Tom/WT}$ mice. **f**, Violin plots displaying expression levels of indicated genes across clusters (top row) and their associated representative FACS plots showing protein expression within hepatic ILC1 (bottom row). **g**, Frequency of IFN-γ-, TNF- and GM-CSF-producing cells within CD127⁺ and CD127⁻ liver ILC1 and NK cells of WT mice 4 hours after in vitro stimulation with PMA/Ionomycin and Brefeldin A. Data are representative of 2 independent experiments with $n = 5$ mice per experiment. **h**, In vitro killing of YAC target cells by CD127⁺ and CD127⁻ liver ILC1 and NK cells at indicated target:effector ratios. Data are representative of three independent experiments with two to three replicates per condition. Bar graphs indicate individual mice (symbols) and means (bar), error bars display means ± s.d. Statistical significance was calculated by unpaired two-tailed *t*-test; $^*P < 0.05$, $^{**}P < 0.01$, $^{***}P < 0.001$, $^{****}P < 0.0001$; n.s., not significant.

which are characteristically expressed in ILC progenitors[4,6,25,28,29]. StemID trajectory analysis suggested a model of ILC1 differentiation in which cells represent early maturation stages that gradually downregulate *Il7r*, *Il18r1*, *Tcf7*, *Kit*, *Emb*, *Rora*, and *Ikzf2*, while gaining expression of *Itgax*, *Cd200r2*, *Cd3g*, and genes encoding a range of effector molecules including *Fgl2*, *Ccl5*, *Gzma*, and *Gzmb* (Fig. 3c). As inferred from the RaceID3 analysis, flow cytometric analysis identified a cKit⁺CD127^{hi}IL-18R1^{hi}TCF-1^{hi} subset of ILC1s

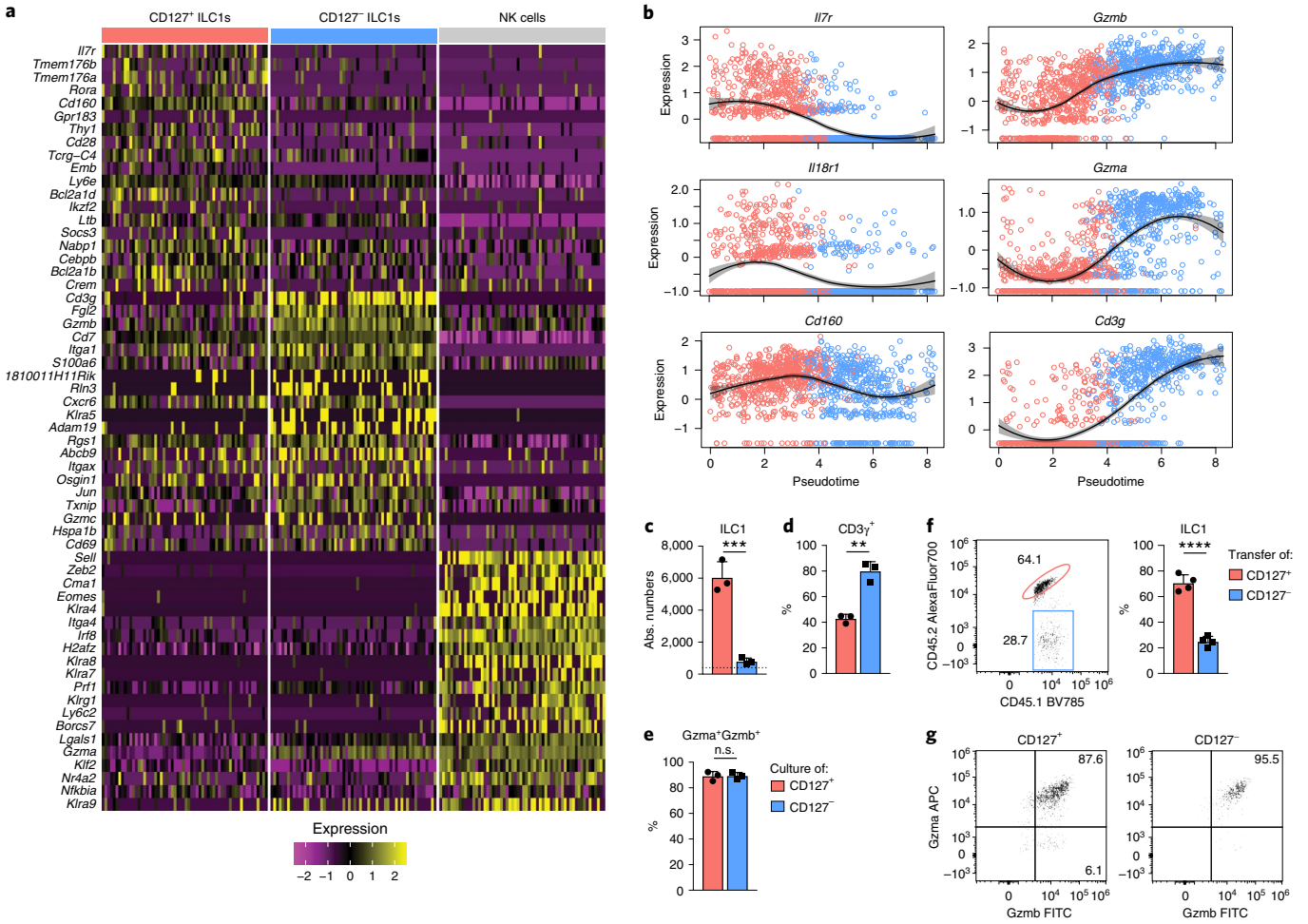

Fig. 2 | CD127⁺ ILC1s are precursors of CD127⁻ cytotoxic-like ILC1s. a, Heat map of marker gene expression associated with identified clusters of scRNA-seq analysis depicted in Fig. 1c. The color scale represents *z* scores of gene expression. **b**, Pseudotemporal ordering of ILC1 single-cell transcriptomes with Slingshot. Expression of selected genes along the pseudotime. Colors indicate cluster identity as in Fig. 1c. Black curve shows the local polynomal regression of the distribution and gray area the confidence interval. **c**–**e**, In vitro culture of CD127⁺ and CD127⁻ liver ILC1s with IL-2 and OP9-DL1 cells for 7 days. Absolute ILC1 numbers (**c**) and the frequencies of CD3γ⁺ (**d**) and Gzma⁺Gzmb⁺ (**e**) cells on day 7 are shown. The dashed line indicates number of cells on day 0 (input = 400 cells). Data are representative of 3 independent experiments with $n = 3$ replicates per experiment (**c**–**e**). **f**,**g**, Results from in vivo cotransfer of congenically marked CD127⁺ and CD127⁻ liver ILC1s into sublethally irradiated *Rag2*$^{-/-}\gamma c^{-/-}$ mice. Representative FACS analysis and bar graphs show the relative frequency (**f**) and granzyme expression (**g**) of liver ILC1s derived from the indicated transferred ILC1 subsets on day 15. Data are representative of 2 independent experiments with $n = 4$ mice (**f**,**g**). Bar graphs indicate replicates (**c**–**e**) or individual mice (**f**) (symbols) and mean (bar), error bars display means ± s.d. Statistical significance was calculated by unpaired two-tailed *t*-test; $^{**}P < 0.01$, $^{***}P < 0.001$, $^{****}P < 0.0001$.

that represented about 10% to 15% of hepatic ILC1s (Fig. 3d). Furthermore, we could demonstrate, at the protein level, the predicted expression gradients of CD127, IL-18R1, TCF-1, Gzma, Gzmb, and CD3γ marker genes along the proposed developmental path from cKit⁺CD127⁺ toward cKit⁻CD127^{int} and finally cKit⁻CD127⁻ ILC1s (Fig. 3e). Confirming their potential for effector maturation along this trajectory, sort-purified cKit⁺CD127⁺ ILC1s lost CD127 and IL-18R1 expression and gained high expression of granzymes upon in vitro culture (Fig. 3f and Extended Data Fig. 3h). Of note, cKit⁺CD127⁺ ILC1s dramatically outcompeted the cKit⁻ ILC1 subsets in their potential to generate progeny effector ILC1s, consistent with the idea that a 'progenitor-like' transcriptional program endows these cells with an increased expansion and differentiation potential.

TCF-1^{hi} early ILC1s are lineage-committed effector cells. The TCF-1^{hi} early-stage ILC1s identified here expressed several genes that are also expressed in ILCPs and exhibit a marked expansion potential, raising the question whether these cells represent progenitor-like or lineage-committed cells. In contrast to ILCPs, cKit⁺TCF-1^{hi} ILC1s expressed NK1.1, NKp46, and T-bet and produced IFN-γ upon stimulation (Fig. 4a,b). Interestingly, we found that TCF-1^{hi} ILC1s expressed Hobit, suggesting that expression of Hobit was specifically acquired at this early differentiation stage of ILC1s (Fig. 4c). Hobit expression was absent in ILCPs in bone marrow and in Lin⁻CD127⁺NK1.1⁻ liver cells, which contain hepatic ILC2s and ILC3s as well as cells with a cKit⁺IL-18R1⁺TCF-1^{hi} phenotype that is characteristic of circulating and tissue-associated ILCPs[4–6]. We also failed to detect Hobit reporter activity in recently discovered liver-resident lineage Sca1⁺Mac-1⁺ (LSM) cells that may contribute to the local differentiation of ILC1s (ref. [30]) (Fig. 4d–g). To test the developmental potential of Hobit-expressing cells, we took advantage of the Hobit-driven Cre recombinase of Hobit reporter mice by crossing these mice onto ROSA26–flox-stop-flox-eYFP (ROSA26–eYFP) mice. The Hobit-driven Cre recombinase will excise the floxed transcriptional stop sequence and enable fate mapping of Hobit expression through constitutive eYFP expression.

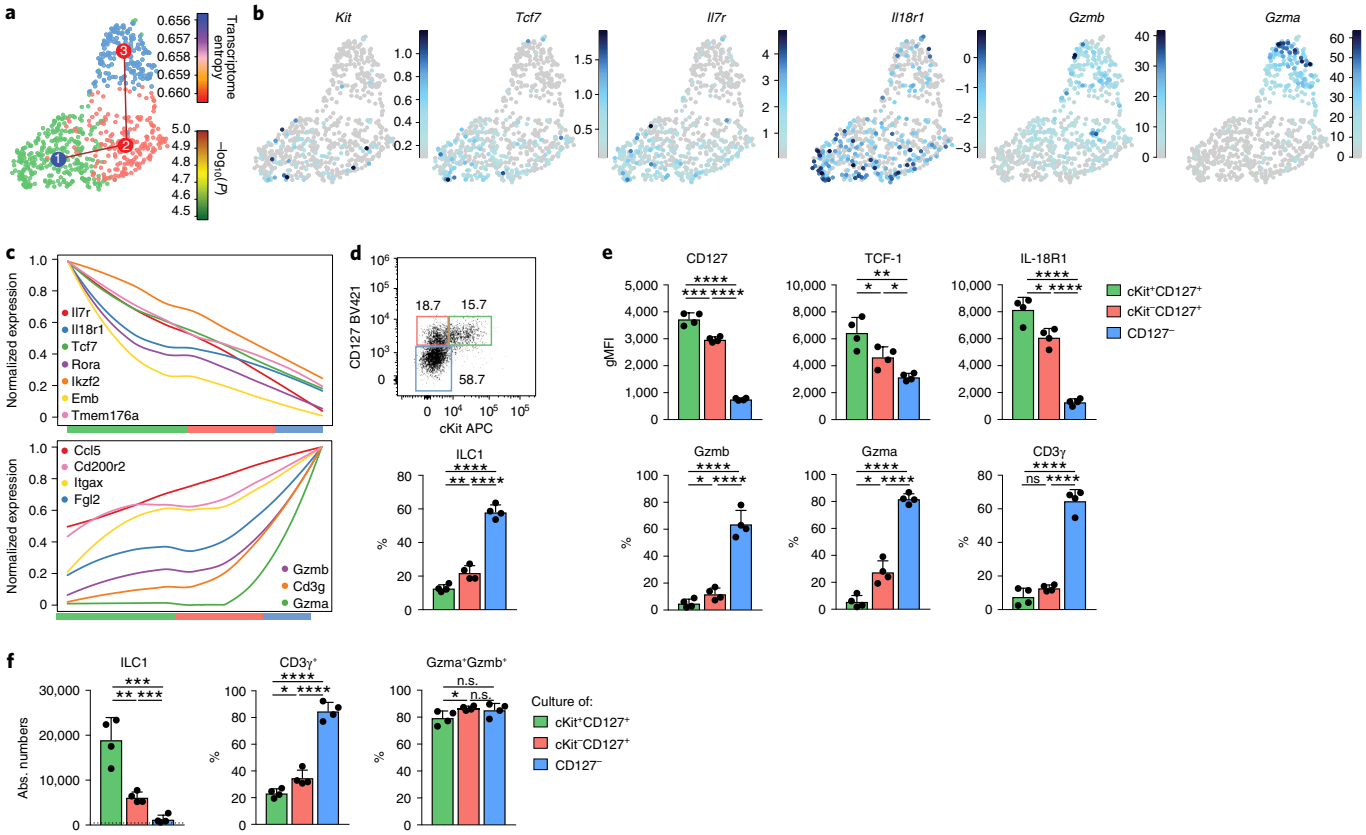

Fig. 3 | TCF-1^{hi} early ILC1s give rise to downstream effector ILC1s. a–**c**, scRNA-seq analysis of hepatic ILC1s. **a**, UMAP visualization of single-cell liver ILC1 transcriptomes clustered with RaceID3 and overlaid with lineage inference using StemID2. Node color depicts transcriptome entropy and link color indicates the *P* value of StemID2 links ($P < 0.05$, Methods). **b**, UMAP visualization showing $\log_2$-normalized expression of selected genes. **c**, Pseudotemporal gene-expression profile of indicated marker genes of *Tcf7*^{hi} (left) and *Tcf7*^{lo} ILC1 (right) along the inferred differentiation. Color bars indicate cluster identity. **d**,**e**, Representative FACS analysis of hepatic ILC1 subsets based on CD127 and cKit expression. Histogram indicates the relative abundance within liver ILC1 (**d**). gMFI of CD127, TCF-1 and IL-18R1 expression within ILC1 subsets (top) and the frequency of Gzmb-, Gzma- and CD3γ-positive cells within indicated ILC1 subsets (bottom) (**e**). **f**, In vitro culture of sort-purified indicated hepatic ILC1 subsets cultured in the presence of IL-2 and OP9-DL1 cells for 7 days. The absolute numbers and frequency of CD3γ$^+$ and Gzma$^+$Gzmb$^+$ cells on day 7 are shown. The dashed line indicates the number of cells on day 0 (input = 400 cells). Data are representative of 3 independent experiments (**d**–**f**) with $n = 3$ mice per group (**d**,**e**) or $n = 4$ replicates per experiment (**f**). Bar graphs indicate individual mice (**d**,**e**) or replicates (**f**) (symbols) and mean (bar); error bars display means ± s.d. Statistical significance was calculated by unpaired two-tailed *t*-test; $^*P < 0.05$, $^{**}P < 0.01$, $^{***}P < 0.001$, $^{****}P < 0.0001$.

Previous analysis has shown the efficacy and specificity of these Hobit-lineage tracer mice in T cells[17]. Both Hobit reporter activity and Hobit fate mapping were largely absent in ILC lineages, other than ILC1s, in the liver (Fig. 4h–j). As ILC2s and ILC3s are relatively rare cells in the liver, we confirmed these findings in the mesenteric lymph nodes (mLNs) (Fig. 4k–m). These data demonstrate that our analysis identified TCF-1^{hi} early yet lineage-committed differentiation stages of effector ILC1s.

Hobit drives the effector differentiation of committed ILC1s. Mice lacking the transcription factor Hobit are characterized by a paucity of hepatic ILC1s while having normal development of NK cells, which we confirmed using two novel mouse strains (Fig. 5a and Extended Data Fig. 4a–c). Importantly, the few ILC1s detectable in Hobit-deficient mice were not 'ex-ILC3,' as they showed the same level of *Rorc* fate mapping as did ILC1s in WT livers (Extended Data Fig. 4d). To investigate whether Hobit deficiency globally reduced ILC1 numbers or specifically impacted ILC1 development along the newly identified differentiation stages, we sorted Hobit$^+$ ILC1s from Hobit-sufficient (Hobit$^{Tom/WT}$) versus Hobit-deficient (Hobit$^{Tom/KO}$) mice and performed scRNA-seq (Fig. 5b and Extended Data Fig. 4e–g). Our analysis revealed three clusters with gene-expression patterns reminiscent of the findings in WT ILC1s. Interestingly, Hobit-deficient ILC1s accumulated as *Kit*$^+$*TCF-7*^{hi} early ILC1s expressing high levels of *Il7r*, *Il18r1*, *Ikfz2*, *Rora*, and *Emb* (cluster 0, Fig. 5b–d and Extended Data Fig. 4g), while few Hobit-deficient ILC1s expressed *Cd3g* and effector molecules *Ccl4*, *Ccl5*, *Fgl2*, *S100a6*, *Gzma*, and *Gzmb* (cluster 1; Fig. 5b,d and Extended Data Fig. 4g). These data suggested a developmental block of ILC1 differentiation in the absence of Hobit. FACS analysis confirmed the inferred phenotypes of Hobit-deficient ILCs, highlighting a close correlation between single-cell messenger RNA (mRNA) and protein expression (Fig. 5e–g). Again, trajectory analysis suggested that cKit$^+$CD127^{hi}IL-18R1^{hi}TCF-1^{hi} subsets, which accumulated in the absence of Hobit, have the potential to mature toward CD127^{int}TCF-1^{int} and CD127$^-$TCF-1$^-$ ILC1s and to concomitantly expand the expression of effector molecules (Extended Data Fig. 5h,i). Interestingly, cKit$^+$TCF-1^{hi}CD127^{hi}IL-18R1^{hi} early ILC1s were present at normal numbers in Hobit-deficient mice (Fig. 5h,i). In contrast, cKit$^-$CD127$^+$, and particularly CD127$^-$ ILC downstream differentiation stages, were severely reduced in the absence of Hobit (Fig. 5h,i). These phenotypes were cell-intrinsic, as the developmental block of ILC1s in Hobit^{KO} animals was similarly detected in the Hobit-deficient compartment of Hobit^{KO} + Hobit^{WT} mixed bone

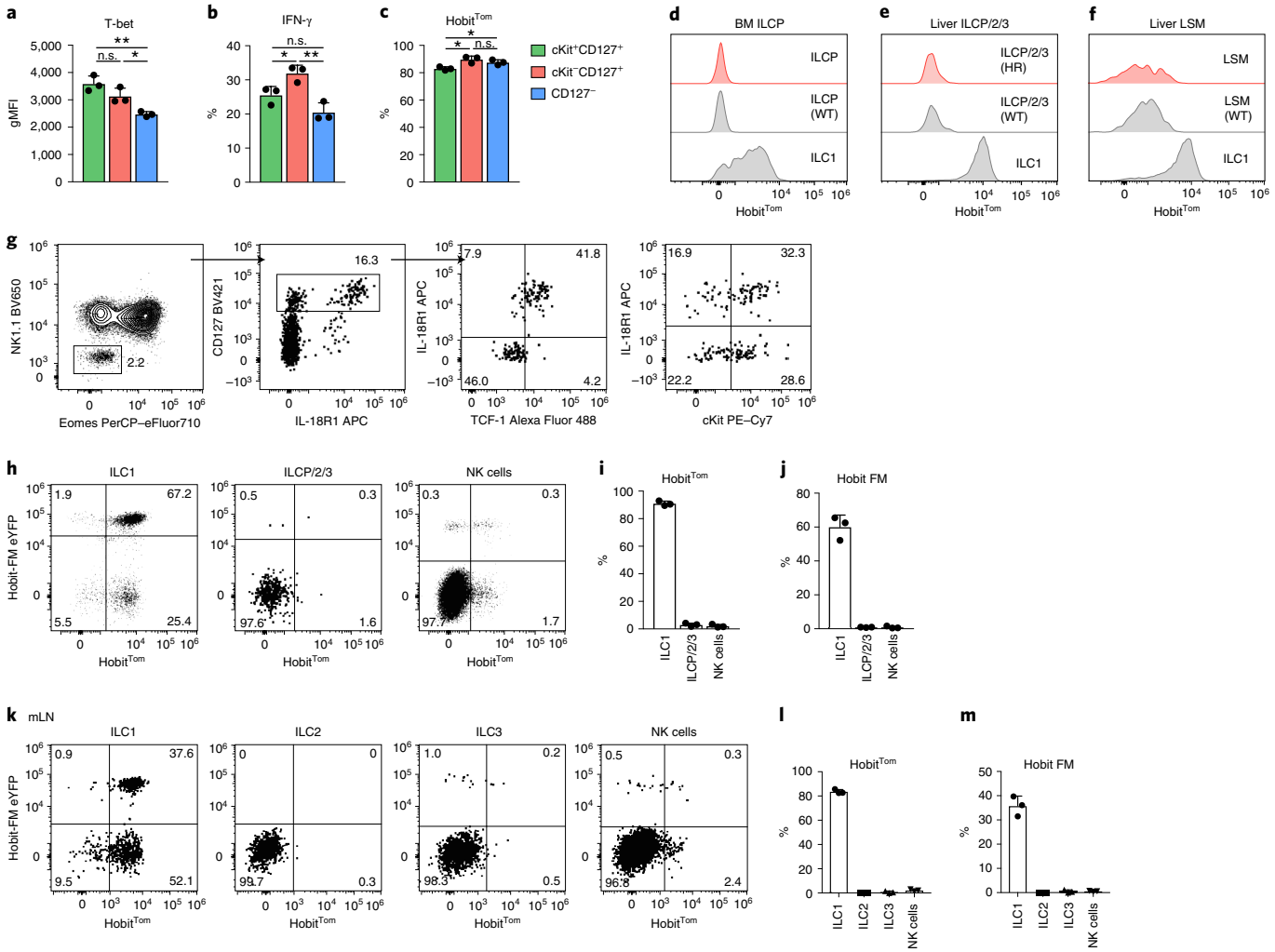

Fig. 4 | Hobit marks lineage-committed ILC1s. a, gMFI of T-bet expression within subsets of hepatic ILC1. **b**, The frequency of IFN-γ-producing cells within the indicated subsets 4 hours after in vitro stimulation with IL-12, IL-18 and Brefeldin A. **c**, The frequency of Hobit-positive ILC1s within the indicated subsets. **d**–**f**, Representative histograms showing the expression of Hobit^{Tom} in indicated cell types in bone marrow (BM) and livers of WT and Hobit$^{Tom/WT}$ mice. BM ILCPs were gated as Lin$^-$NK1.1$^-$CD127$^+$IL-18R1$^+$ST2$^-$ cells. BM ILC1s were gated as Lin$^-$NK1.1$^+$NKp46$^+$CD49a$^+$CD49b$^-$ cells. A gate containing Lin$^-$NK1.1$^-$CD127$^+$ putative liver ILCPs, ILC2 (ILCP/2/3), was used as depicted in **g**. Liver LSMs were gated as Lin$^-$NK1.1$^-$NKp46$^-$CD11b$^+$Sca1$^+$ cells. **g**, The gating strategy used to identify and phenotype Lin$^-$NK1.1$^-$CD127$^+$ liver ILCP/2/3. **h**–**m**, Representative FACS analysis of Hobit^{Tom} and Hobit^{eYFP} fate-map (FM) labeling across different ILC lineages in the liver (**h**–**j**) and mLNs (**k**–**m**). ILC2s were gated as Lin$^-$NK1.1$^-$NKp46$^-$CD127$^+$KLRG1$^+$ cells. ILC3s were gated as Lin$^-$NK1.1$^-$NKp46$^-$CD127$^+$KLRG1$^-$CD90$^+$ cells. Data are representative of 3 (**a**,**c**,**e**,**g**) or 2 (**b**,**d**,**f**,**h**–**m**) independent experiments with $n = 3$ mice per experiment. Bar graphs indicate individual mice (symbols) and mean (bar); error bars display means ± s.d. Statistical significance was calculated by unpaired two-tailed *t*-test; $^*P < 0.05$, $^{**}P < 0.01$.

marrow chimeric mice (Extended Data Fig. 5a–c). Together, these analyses suggest that cKit$^+$TCF-1^{hi}CD127^{hi}IL-18R1^{hi} cells represent an early developmental stage of ILC1s that initiates Hobit expression to drive their effector differentiation and diversification.

The markedly increased expression of *Tcf7*, *Rora*, *Il18r1*, and *Kit* urged us to address whether WT or Hobit-deficient TCF-1^{hi} early ILC1s resembled ILCPs. To this end, we selected a list of ILCP signature genes on the basis of several recent studies[4,25,28,29] and calculated expression scores in the ILC1 clusters identified in our scRNA-seq analysis. These comparisons yielded a low ILCP score for all hepatic ILC1 subsets, but readily identified ILCPs in a dataset recently published by Harly et al.[29] (Fig. 6a–d). The unbiased derivation of an ILCP core signature from this dataset yielded similar results (Extended Data Fig. 5d–g). Consistently, while some 'ILCP genes' were indeed enriched in TCF-1^{hi} early ILC1s, they largely lacked expression of other genes associated with ILCPs, such as *Tox2*, *Zbtb16*, *Bcl11b*, *Pdcd1*, *Lef1*, *Myb*, and *Rxrg*. Instead, all Hobit-deficient and Hobit-sufficient ILC1 subsets expressed ILC1 marker genes that were not detected in ILCPs. As in WT mice, Hobit-deficient TCF-1^{hi} ILCs had a CD200r$^+$T-bet$^+$Rorγt$^-$Hobit^{Tom+} phenotype and expressed IFN-γ upon stimulation (data not shown). These data demonstrate that Hobit does not contribute to the commitment of ILCP to the ILC1 lineage but specifically acts in lineage-committed ILC1s to regulate their effector differentiation.

Hobit regulates ILC1 effector states in adult life. To identify putative targets of Hobit in ILCs, we matched our gene-expression data with Hobit chromatin-binding sites established through Hobit chromatin immunoprecipitation and sequencing (ChIP–seq) in T cells[16]. Hobit has been suggested to directly regulate the expression of genes associated with T cell stemness (that is, the capacity to expand and generate downstream effector cells), including *Tcf7*,

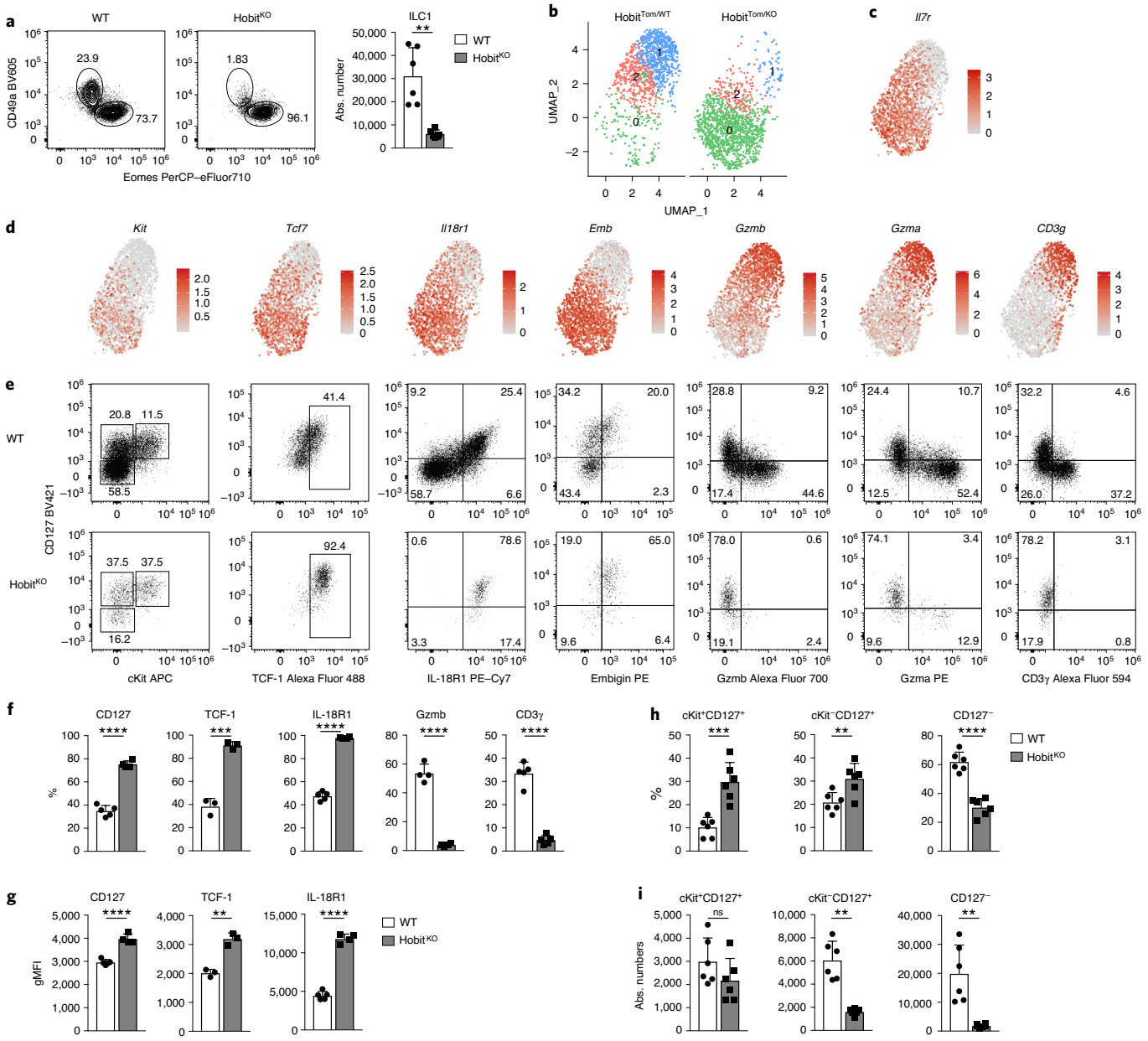

Fig. 5 | Hobit drives the effector differentiation of lineage-committed ILC1s. a, Representative FACS analysis displaying Lin$^-$NK1.1$^+$ hepatic ILC1s and NK cells in WT and Hobit^{KO} mice. Bar graphs indicate absolute numbers of liver ILC1s. **b**–**d**, scRNA-seq analysis of 2,549 hash-tagged liver ILC1s sorted from Hobit$^{Tom/WT}$ and Hobit$^{Tom/KO}$ mice. UMAP visualization of liver ILC1 clusters (**b**), colored according to the normalized expression of selected genes (**c**,**d**). **e**–**g**, Representative FACS analysis of the expression of indicated markers by ILC1s from livers of WT and Hobit^{KO} mice. **f**, Frequency of ILC1s expressing indicated marker proteins of WT and Hobit^{KO} mice. **g**, gMFI of CD127, TCF-1, and IL-18R1 expression within marker-positive ILC1s. **h**,**i**, Frequency (**h**) and absolute numbers (**i**) of indicated ILC1 subsets in WT and Hobit^{KO} mice. Data in **a**, **h** and **i** are pooled from 2 independent experiments with $n = 3$ mice per group. Data in **f** and **g** show 1 representative of 3 independent experiments with $n = 3$, 4, and 5 mice per group. Bar graphs indicate individual mice (symbols) and means (bar), error bars display means ± s.d. Statistical significance was calculated by unpaired two-tailed *t*-test; $^{**}P < 0.01$, $^{***}P < 0.001$, $^{****}P < 0.0001$.

Bach2, and *Batf3* (refs. [16,31,32]). Interestingly, we found that expression of these genes was increased in Hobit-deficient ILC1s and was downregulated along the transition of cKit$^+$TCF-1^{hi}CD127^{hi} to cKit$^-$TCF-1^{int}CD127^{int} ILC1s, consistent with the idea that Hobit regulates ILC1 'stemness' versus effector differentiation by modulating these genes (Fig. 6e,f).

ILCs differentiate during the first weeks of life, after which they persist largely as tissue-resident populations that can self-renew, potentially through maturation from local progenitors[4,5,13,33,34]. To test whether Hobit acted during an early developmental window, or whether continued expression of Hobit was required for the regulation of ILC1 effector states in the adult organism, we generated Ubi$^{Cre-ERT2}$ Hobit$^{fl/fl}$ mice (Fig. 6g–i). Conditional deletion of Hobit increased expression of TCF-1, IL-18R1, and CD127 and the frequency of cKit$^+$TCF-1^{hi} and CD127$^+$ ILC1s while reducing the frequency of CD127$^-$ granzyme-expressing cells. Although this analysis cannot formally distinguish between the reversion of CD127$^-$TCF-1^{lo}Gzm^{hi} ILC1s to CD127$^+$TCF-1^{hi}Gzm^{lo} ILC1s after conditional Hobit ablation versus the accumulation of CD127$^+$TCF-1^{hi}Gzm^{lo} ILC1s caused by a blockade to differentiate

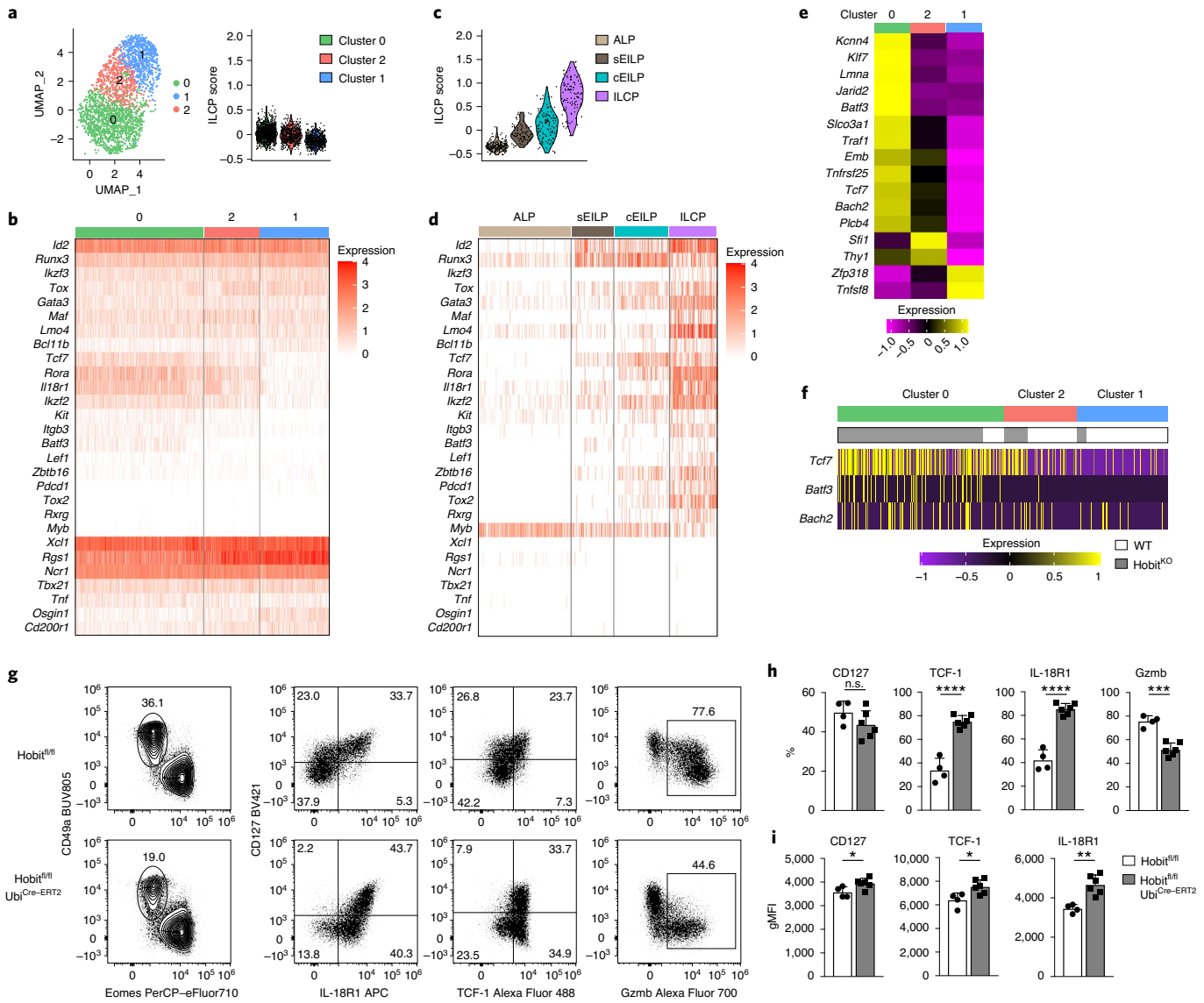

Fig. 6 | Hobit is continuously required to regulate the differentiation of TCF-1^{hi} Gzm^{lo} versus TCF-1^{lo} Gzm^{hi} effector ILC1s. a–d, UMAP visualization of liver ILC1 clusters as in Fig. 5b. Violin plots display ILCP score calculation of selected ILCP genes across identified clusters (**a**) and in a scRNA-seq dataset of indicated BM progenitors generated by Harly et al.[29] (**c**). **b**,**d**, Heat maps of marker gene expression associated with ILCPs across identified (**b**) and published (**d**) clusters. ALP, all-lymphoid progenitors; sEILP, specific early innate lymphoid progenitors; cEILP, committed early innate lymphoid progenitors; ILCP, innate lymphoid progenitors. **e**, Heat map of expression of potential Hobit target genes (derived from Mackay et al.[16] ChIP–seq data of T cells) across identified clusters. **f**, Expression of *Tcf7*, *Batf3* and *Bach2* within liver ILC1s from WT and Hobit^{KO} mice. **g–i**, Representative FACS analysis of liver ILC1 in Ubi$^{Cre-ERT2}$ Hobit$^{fl/fl}$ mice and littermate controls on day 35 after tamoxifen treatment, gated on Lin$^-$NK1.1$^+$ cells (left) and ILC1s (**g**). Frequency of indicated marker-positive cells within ILC1 (**h**) and gMFI of CD127, TCF-7 and IL-18R1 expression within marker-positive liver ILC1s (**i**). Data show 1 representative of 3 individual experiments with $n = 4$ or 6 mice per group (**g–i**). Bar graphs indicate individual mice (symbols) and mean (bar), error bars display means ± s.d. Statistical significance was calculated by unpaired two-tailed *t*-test; $^*P < 0.05$, $^{**}P < 0.01$, $^{***}P < 0.001$, $^{****}P < 0.0001$.

into CD127$^-$TCF-1^{lo}Gzm^{hi} ILC1 after Hobit ablation, these data suggest that hepatic ILC1s continuously require Hobit expression to regulate the balanced differentiation between TCF-1^{hi}Gzm^{lo} and TCF-1^{lo}Gzm^{hi} effector ILC1s.

Hobit drives ILC1 effector differentiation across tissues. Our data revealed that Hobit drives the differentiation of TCF-1^{hi} early ILC1s into defined stages of effector ILC1s in the liver. To test whether ILC1s in other tissues also expressed Hobit and similarly segregated into distinct subsets along the identified differentiation trajectory, we analyzed ILC1s in salivary glands (SG), kidneys, mLNs, and small intestinal lamina propria (SI). In all of these tissues, NK1.1$^+$Eomes$^-$CD49a$^+$ ILC1s expressed Hobit (Fig. 7a). The degree of effector maturation, however, dramatically varied across organs. Reminiscent of cells in the liver, ILC1s in the SG comprised IL-18R1$^+$Gzmb$^-$ as well as IL-18R1$^-$Gzmb$^+$ cells (Fig. 7b,c and Extended Data Fig. 6). In contrast, the majority of ILC1s in the kidney, mLNs, and SI lacked expression of Gzmb and were characterized by a CD127$^+$IL-18R1$^+$ phenotype (Fig. 7b,c and Extended Data Fig. 6). Similar to cells in the liver, IL-18R1$^-$Gzmb$^+$ and IL-18R1$^-$CD3γ$^+$ ILC subsets were strongly reduced in all analyzed organs of Hobit-deficient mice, while TCF-1 expression and the frequency of CD127^{hi}TCF-1^{hi}IL-18R1^{hi} ILC1s was increased (Fig. 7b,c and Extended Data Fig. 6). Consistent with a cell-intrinsic

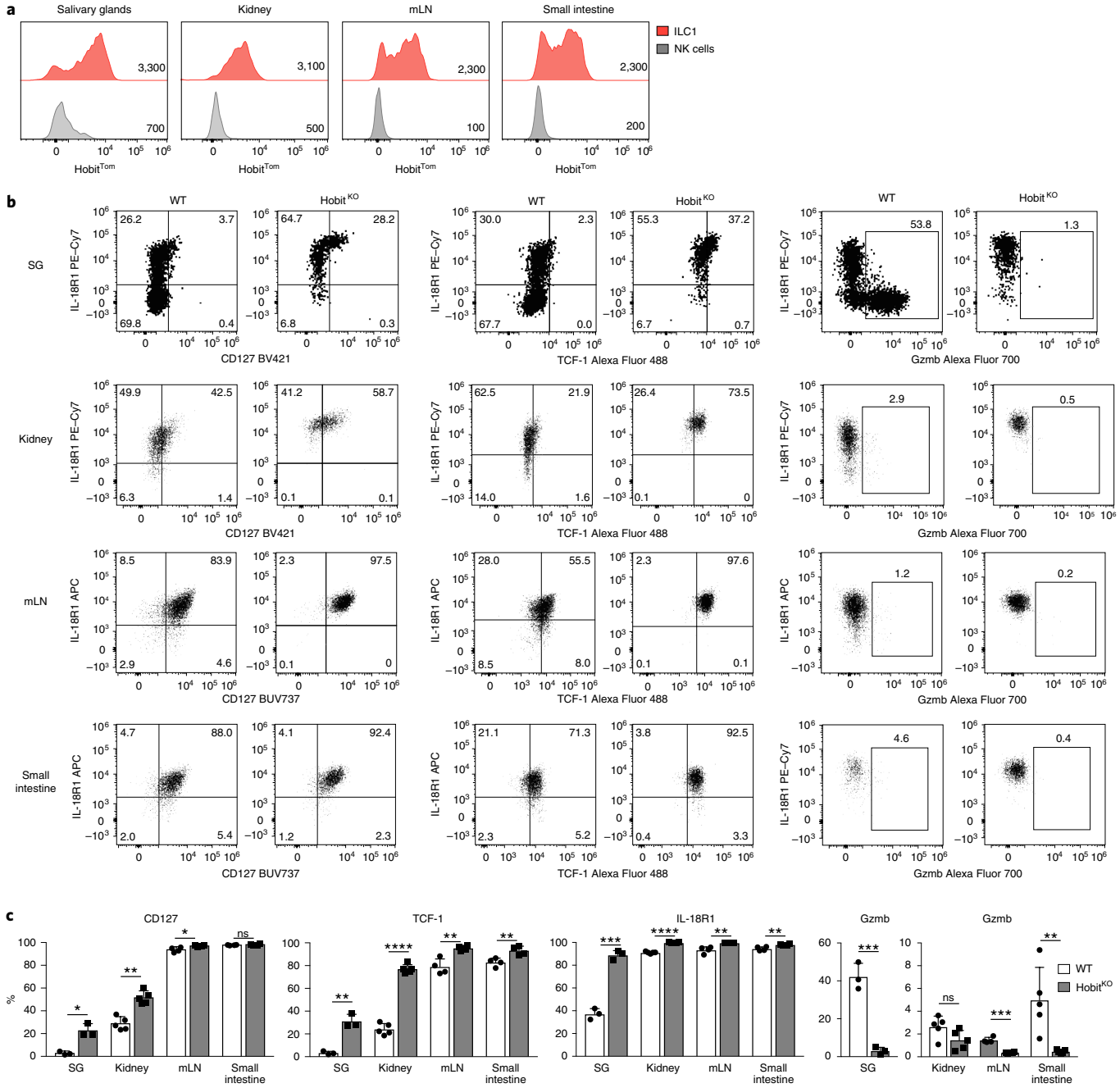

Fig. 7 | Effector differentiation of ILC1s is regulated by Hobit across tissues. a, Representative histograms displaying Hobit^{Tom} signal in ILC1s and NK cells isolated from indicated organs of Hobit$^{Tom/WT}$ mice. To maintain the reporter signal, ILC1s in SG and kidney were gated as Lin$^-$NK1.1$^+$NKp46$^+$CD49a$^+$DX5$^-$ cells; in the mLNs and SI, ILC1s were gated as Lin$^-$NK1.1$^+$NKp46$^+$CD127$^+$CXCR6$^+$ cells, as shown in Extended Data Fig. 6a. Data are representative of 2 individual experiments with $n = 3$–4 mice per group. **b**,**c**, Representative FACS analysis of indicated marker expression of Lin$^-$NK1.1$^+$CD49a$^+$Eomes$^-$RORγt$^-$ ILC1s from the indicated organs of WT and Hobit^{KO} mice (**b**). Frequency of ILC1s expressing the indicated marker proteins in WT and Hobit^{KO} mice (**c**). Data in **b** and **c** show 1 representative of 3 independent experiments with $n = 3$ (SG), 4 (mLN, small intestine) and 5 (kidney) mice per group. Bar graphs indicate individual mice (symbols) and mean (bar), error bars display means ± s.d. Statistical significance was calculated by unpaired two-tailed *t*-test; $^*P < 0.05$, $^{**}P < 0.01$, $^{***}P < 0.001$, $^{****}P < 0.0001$.

function of Hobit in these cells, the expression levels of CD127, IL-18R1, and TCF-1 increased in the absence of Hobit in all analyzed organs in mixed bone marrow chimeric mice (Extended Data Fig. 7a–f). As in the liver, Hobit expression was continuously required to regulate expression of TCF-1 and granzymes (Extended Data Fig. 7g–j). Together, these data identify Hobit as a key transcriptional regulator of ILC1 differentiation across all analyzed organs.

In addition to Eomes$^-$ ILC1s, the SG is populated by Eomes$^+$CD49a$^+$ tissue-resident NK cells that share similarities with cNK cells and with ILC1s (ref. [35]). Reminiscent of Eomes$^-$ bona-fide ILC1s in SG and liver, these Eomes$^+$CD49a$^+$ SG cells expressed Hobit and could be divided into TCF-1^{hi}IL-18R1^{hi} and TCF-1$^-$IL-18R1$^-$CD3γ$^+$ and/or Gzmb$^+$ subsets (Extended Data Fig. 8a–e). Again, Hobit was required for the differentiation of CD3γ- and Gzmb-expressing cells. In the absence of Hobit, differentiation

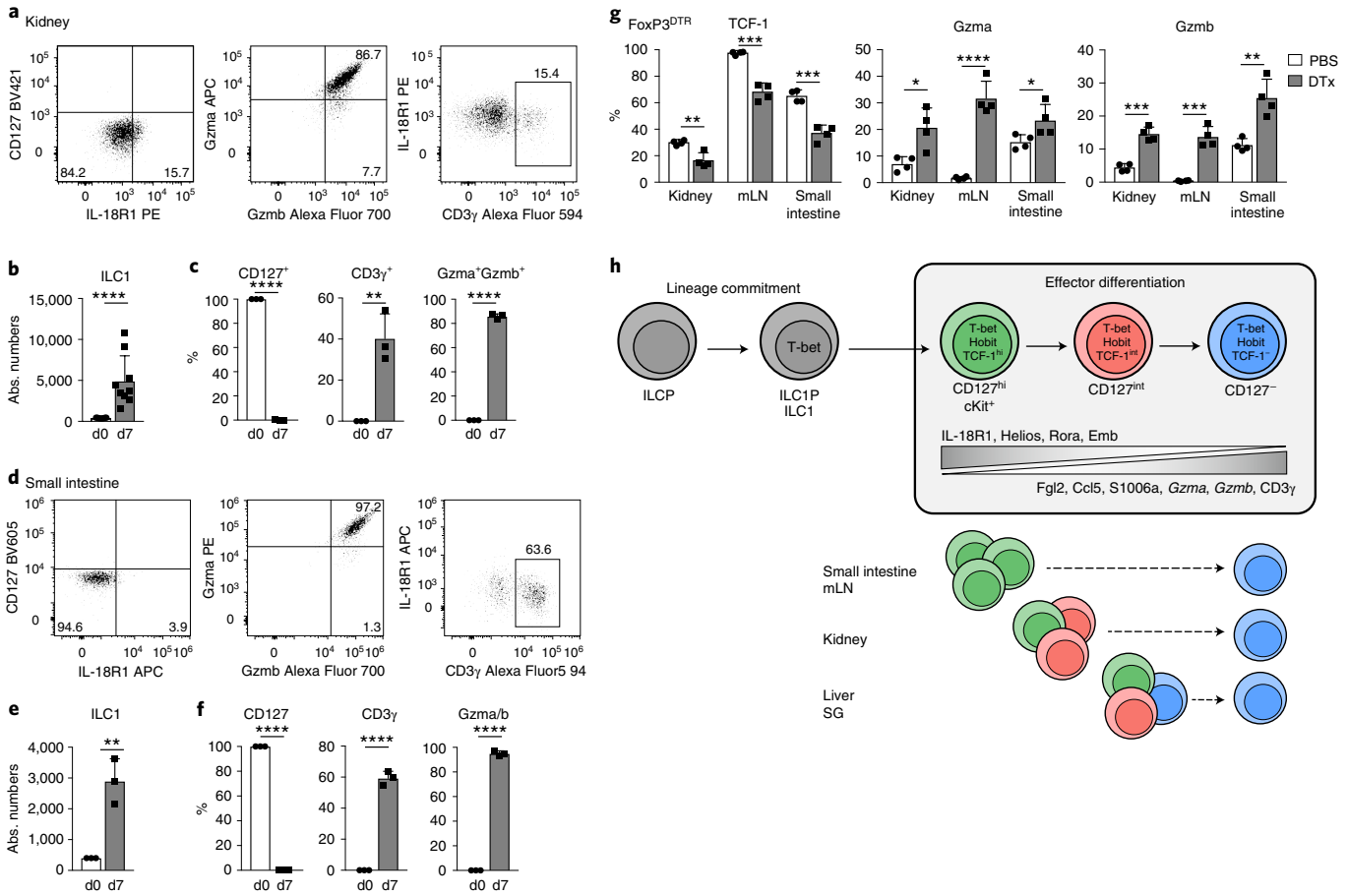

Fig. 8 | The developmental potential of ILC1s is conserved across tissues. a–f, In vitro culture of CD127$^+$ kidney (**a**–**c**) and small intestinal (**d**–**f**) ILC1s in the presence of IL-2 and OP9-DL1 feeder cells. **a**,**d**, Representative FACS plots on day 7. **b**,**e**, Absolute numbers of cells on day 0 (input = 400 cells) and day 7. **c**,**f**, Frequency of CD127$^+$, CD3γ$^+$ and Gzma$^+$Gzmb$^+$ cells. Data are representative of 3 independent experiments with $n = 3$ replicates per experiment. **g**, FACS analysis of ILC1s from indicated organs of T_{reg} cell-depleted or mock-treated FoxP3^{DTR} mice on day 8 of DT treatment (DTx). Bar graphs indicate the frequency of ILC1s expressing indicated proteins. Data are representative of 3 independent experiments with $n = 4$ mice per group. **h**, Schematic summarizing sequential mechanisms of ILC1 lineage commitment and effector differentiation downstream of TCF-1^{hi} early ILC1s, which is transcriptionally regulated by Hobit. ILC1s across tissues have a uniform capacity to differentiate toward TCF-1^{lo}Gzm^{hi} cells. Bar graphs indicate replicates (**b**,**c**,**e**,**f**) or individual mice (**g**) (symbols) and mean (bar), error bars display means ± s.d. Statistical significance was calculated by unpaired two-tailed *t*-test; $^*P < 0.05$, $^{**}P < 0.01$, $^{***}P < 0.001$, $^{****}P < 0.0001$.

of Eomes$^+$CD49a$^+$ cells was stalled at the IL-18R1^{hi}TCF-1^{hi} stage. Although Eomes$^+$CD49a$^+$ SG cells lacked expression of CD127, as previously reported[35,36], these data reveal intriguing parallels of the phenotype, differentiation stages, and transcriptional requirements of Eomes$^+$ and Eomes$^-$ tissue-resident NK cells and ILCs, and demonstrate that Hobit is a critical determinant of effector differentiation of these group 1 ILCs.

ILC1 developmental potential is conserved across tissues. The observation that the ILC1 compartment in kidney, mLN, and SI was largely devoid of IL-18R1$^-$Gzmb$^+$ cytotoxic-like populations (Fig. 7b,c) raised the question whether ILC1s in these organs are 'halted' in a less mature differentiation state, potentially owing to the paucity of local signals that would drive their differentiation into cytotoxic-like cells, or whether these ILC1s intrinsically lack such developmental potential. To distinguish between these possibilities, we sort-purified CD127$^+$ ILC1s from kidney and SI and cultured them on OP9-DL1 feeder cells. Interestingly, CD127$^+$ ILC1s isolated from both organs, but not ILC3, readily expanded and gave rise to CD127$^-$ ILC1s that expressed CD3γ and/or granzymes (Fig. 8a–f, Extended Data Fig. 8f, and data not shown), similar to CD127$^+$ hepatic ILC1s (Fig. 2c–e). These data suggested that these ILC1s can undergo further effector differentiation but may be halted in their differentiation owing to the lack of activating signals or the active suppression in their respective tissue niches. To test whether ILC1s can undergo further effector differentiation in these organs in vivo, we depleted regulatory T (T_{reg}) cells, which creates an inflammatory setting to which ILC1s respond locally, as tissue-resident cells[33]. Intriguingly, we found that T_{reg} depletion promoted the effector differentiation of ILC1s in all analyzed tissues, as evidenced by the downregulation of TCF-1 and the concomitant increase in Gzma and Gzmb expression (Fig. 8g and Extended Data Fig. 8f). Together, these data reveal that the cell-intrinsic differentiation potential of ILC1s is conserved across tissues and suggest that signals perceived from the microenvironment regulate the Hobit-dependent effector differentiation of ILC1s in specific tissue niches.

Discussion

These findings reveal a uniform pathway of ILC1 effector differentiation conserved across tissues and sequential mechanisms of ILC1 lineage polarization and effector differentiation. Our analyses define early TCF-1^{hi} committed ILC1s that undergo Hobit-dependent

maturation into distinct populations that segregate by proliferative potential and expression of effector molecules. These remarkable parallels to the population structure of antigen-experienced T cells and cNK cells suggest that key principles in the regulation of polarized lymphocyte populations are conserved among innate and adaptive lymphocytes[37–39].

Our work provides a conceptual complement to the recent identification of tissue-associated multipotent ILC progenitors that can differentiate in situ into ILC1s, ILC2s, and ILC3s (refs. [4,5,7,40]). Although these studies highlight the developmental steps from progenitors toward lineage-committed cells, our work identifies a cascade of differentiation events occurring in committed ILC1s. The analysis of Hobit fate mapping in mice revealed that Hobit-expressing ILC1s do not substantially contribute to the cNK, ILC2, and ILC3 lineages, at least during development and homeostasis, and underlines that Hobit activity is upregulated after commitment to the ILC1 lineage. Conversely, ILC1s in Hobit-deficient mice retained an ILC1 phenotype, suggesting that Hobit acts as a transcriptional regulator of effector differentiation after lineage commitment.

Our analyses establish that heterogeneous subsets of ILC1s that have previously been characterized as organ-specific helper-like versus cytotoxic-like ILC1s are distinct developmental stages connected along a Hobit-dependent differentiation path. Importantly, TCF-1^{hi} early ILC1s already have the ability to produce IFN-γ and other proinflammatory mediators, suggesting that they represent a mature ILC1 subset that can exert effector functions. Downstream differentiation stages appear to retain the potential to release proinflammatory cytokines, but gradually acquire other effector functions such as the production of Fgl2 and granzymes and the ability to efficiently kill target cells.

The identification of Hobit-dependent differentiation stages may also explain why ILC1s in Hobit-deficient mice are not generally reduced in numbers, in contrast to the liver compartment, where lack of Hobit leads to a dramatic reduction in ILC1s. We observed that remaining ILC1s, identified as cKit^{+}TCF-1^{hi} ILC1s, were present in similar numbers in WT and Hobit-deficient livers. The finding that this early ILC1 phenotype dominates in the intestine, kidney and mLNs of SPF mice may explain the relatively minor reduction of ILC1s in these compartments.

Although ILC1s from different tissues preserved the capacity to generate cytotoxic-like cells, our work suggests that the actual differentiation of these effector ILC1s depends on signals from within their tissue environment. Potentially, Hobit has a permissive role and requires independent tissue-specific signals to cooperatively regulate ILC1 effector differentiation. In this regard, it will be interesting to examine whether distinct ILC1 differentiation stages require access to microanatomical niches and interacting cell types that are present in only certain tissues. It will also be important to determine whether differentiation of cytotoxic-like ILC1s from TCF-1^{hi} ILC1s is actively restrained in some tissues, as suggested by our analyses of T_{reg} cell-depleted mice, for example to prevent pathology.

Of note, the acquisition of cytotoxic function has recently been documented in in vitro cultures of human tonsillar CD94^{+} ILC1s in response to IL-12 (ref. [21]). Given that these cells do not express Hobit, and that this differentiation process included the upregulation of Eomes, it is unclear whether it represents the human correlate of the differentiation of committed Eomes^{-} ILC1s that we have investigated here. Hobit is, however, broadly expressed in human intestinal intraepithelial ILC1s and in NK cells as well as subsets of activated effector T cells[41,42]. Therefore, beyond its reported function in tissue residency, Hobit may be a critical differentiation factor of these type-1 polarized lymphocytes, consistent with its role in ILC1s that we identified here. It will be important to investigate the transcriptional programs regulating expansion potential versus effector differentiation in human Hobit^{+} versus Hobit^{-} ILCs and NK cells.

Hobit binds directly into the *Tcf7* locus and suppresses expression of TCF-1 in natural killer T cells[16] and in tissue-resident memory T cells[43]. Underlining these findings, we observed that Hobit repressed TCF-1 expression in ILC1. TCF-1 has critical functions in ILCPs, in immature cNKs cells, and in stem-like memory T cells to maintain their increased potential for expansion and self-renewal, and to inhibit the expression of cytotoxic molecules[29,38,39,44–46]. Therefore, Hobit-driven repression of TCF-1 may extinguish a program of ILC 'stemness' and permit terminal differentiation of ILC1s. The repressive activity of Hobit on other potential regulators of stemness in effector lymphocytes, such as Bach2 and Batf3, may contribute to this terminal regulation of ILC1 differentiation. The instructive signals driving the differentiation of committed ILC1 in vivo remain unclear. Our in vitro cultures suggest that IL-2 and IL-15 can contribute to the transition of helper-like ILC1s into cytotoxic-like ILC1s. IL-2 may be more relevant for ILC1 differentiation under inflammatory conditions as occurs upon depletion of T_{reg} cells, while IL-15 may dominate under homeostatic conditions, as supported by its essential contribution to ILC1 development[11,26]. In preliminary analyses, the phenotype of liver ILC1s was not altered in STAT4-KO and IL-18R1-KO mice, or when we neutralized IL-15 (data not shown). Similarly, hepatic ILC1s had no detectable change in phenotype when lacking *Tgfbr2* (ref. [35]). These observations suggest that these cytokines do not directly maintain or induce Hobit and highlight that additional work will be required to address the instructive signals of Hobit expression and the differentiation of lineage-committed ILC1s.

The cKit^{+}CD127^{hi} early differentiation stage of ILC1s, which we identified across different organs, had a very striking potential to expand in response to homeostatic cytokines and to generate downstream effector ILC1s. These findings suggest that, reminiscent of T cells, ILC1s undergo a differentiation process that compartmentalizes expansion potential and specialized effector functions in order to regulate, at the population level, homeostatic maintenance as well as the generation of a spectrum of effector states. Considering the central function of TCF-1^{hi} stem-like cells in T cell responses to chronic infection, tumors, and checkpoint blockade therapy[39,44–46], the identification of mechanisms driving ILC1 effector generation from TCF-1^{hi} early ILC1s provides an important framework for future studies of ILC1-mediated tissue immunity, inflammatory diseases, and their potential therapeutic targeting.

Online content

Any methods, additional references, Nature Research reporting summaries, source data, extended data, supplementary information, acknowledgements, peer review information; details of author contributions and competing interests; and statements of data and code availability are available at https://doi.org/10.1038/s41590-021-01013-0.

Received: 7 January 2021; Accepted: 30 July 2021;
Published online: 30 August 2021

References

1. Colonna, M. Innate lymphoid cells: diversity, plasticity, and unique functions in immunity. *Immunity* **48**, 1104–1117 (2018).
2. Vivier, E. et al. Innate lymphoid cells: 10 years on. *Cell* **174**, 1054–1066 (2018).
3. Riggan, L., Freud, A. G. & O'Sullivan, T. E. True detective: unraveling group 1 innate lymphocyte heterogeneity. *Trends Immunol.* **40**, 909–921 (2019).
4. Zeis, P. et al. In situ maturation and tissue adaptation of type 2 innate lymphoid cell progenitors. *Immunity* **53**, 775–792.e779 (2020).
5. Ghaedi, M. et al. Single-cell analysis of RORα tracer mouse lung reveals ILC progenitors and effector ILC2 subsets. *J. Exp. Med.* **217**, e20182293 (2020).
6. Lim, A. I. et al. Systemic human ILC precursors provide a substrate for tissue ILC differentiation. *Cell* **168**, 1086–1100 (2017).
7. Lim, A. I. & Di Santo, J. P. ILC-poiesis: ensuring tissue ILC differentiation at the right place and time. *Eur. J. Immunol.* **49**, 11–18 (2019).

8. Stokic-Trtica, V., Diefenbach, A. & Klose, C. S. N. NK cell development in times of innate lymphoid cell diversity. *Front. Immunol.* **11**, 813 (2020).
9. Krabbendam, L., Bernink, J. H. & Spits, H. Innate lymphoid cells: from helper to killer. *Curr. Opin. Immunol.* **68**, 28–33 (2020).
10. McFarland, A. P. et al. Multi-tissue single-cell analysis deconstructs the complex programs of mouse natural killer and type 1 innate lymphoid cells in tissues and circulation. *Immunity* **54**, 1320–1337.e1324 (2021).
11. Daussy, C. et al. T-bet and Eomes instruct the development of two distinct natural killer cell lineages in the liver and in the bone marrow. *J. Exp. Med.* **211**, 563–577 (2014).
12. Weizman, O. E. et al. ILC1 confer early host protection at initial sites of viral infection. *Cell* **171**, 795–808 (2017).
13. Sojka, D. K. et al. Tissue-resident natural killer (NK) cells are cell lineages distinct from thymic and conventional splenic NK cells. *eLife* **3**, e01659 (2014).
14. Takeda, K. et al. TRAIL identifies immature natural killer cells in newborn mice and adult mouse liver. *Blood* **105**, 2082–2089 (2005).
15. Peng, H. et al. Liver-resident NK cells confer adaptive immunity in skin-contact inflammation. *J. Clin. Invest.* **123**, 1444–1456 (2013).
16. Mackay, L. K. et al. Hobit and Blimp1 instruct a universal transcriptional program of tissue residency in lymphocytes. *Science* **352**, 459–463 (2016).
17. Behr, F. M. et al. Tissue-resident memory CD8$^+$ T cells shape local and systemic secondary T cell responses. *Nat. Immunol.* **21**, 1070–1081 (2020).
18. Robinette, M. L. et al. Transcriptional programs define molecular characteristics of innate lymphoid cell classes and subsets. *Nat. Immunol.* **16**, 306–317 (2015).
19. Ducimetiere, L. et al. Conventional NK cells and tissue-resident ILC1s join forces to control liver metastasis. *Proc. Natl Acad. Sci. USA* **118**, e2026271118 (2021).
20. Dadi, S. et al. Cancer immunosurveillance by tissue-resident innate lymphoid cells and innate-like T Cells. *Cell* **164**, 365–377 (2016).
21. Krabbendam, L., Heesters, B. A., Kradolfer, C. M. A., Spits, H. & Bernink, J. H. Identification of human cytotoxic ILC3s. *Eur. J. Immunol.* **51**, 811–823 (2020).
22. Fuchs, A. et al. Intraepithelial type 1 innate lymphoid cells are a unique subset of IL-12- and IL-15-responsive IFN-γ-producing cells. *Immunity* **38**, 769–781 (2013).
23. Bernink, J. H. et al. Human type 1 innate lymphoid cells accumulate in inflamed mucosal tissues. *Nat. Immunol.* **14**, 221–229 (2013).
24. Vonarbourg, C. et al. Regulated expression of nuclear receptor RORγt confers distinct functional fates to NK cell receptor-expressing RORγt$^+$ innate lymphocytes. *Immunity* **33**, 736–751 (2010).
25. Walker, J. A. et al. Polychromic reporter mice reveal unappreciated innate lymphoid cell progenitor heterogeneity and elusive ILC3 progenitors in bone marrow. *Immunity* **51**, 104–118.e107 (2019).
26. Klose, C. S. N. et al. Differentiation of type 1 ILCs from a common progenitor to all helper-like innate lymphoid cell lineages. *Cell* **157**, 340–356 (2014).
27. Grün, D. et al. De novo prediction of stem cell identity using single-cell transcriptome data. *Cell Stem Cell* **19**, 266–277 (2016).
28. Xu, W. et al. An Id2(RFP)-reporter mouse redefines innate lymphoid cell precursor potentials. *Immunity* **50**, 1054–1068.e1053 (2019).
29. Harly, C. et al. The transcription factor TCF-1 enforces commitment to the innate lymphoid cell lineage. *Nat. Immunol.* **20**, 1150–1160 (2019).
30. Bai, L. et al. Liver type 1 innate lymphoid cells develop locally via an interferon-γ-dependent loop. *Science* **371**, eaba4177 (2021).
31. Yao, C. et al. BACH2 enforces the transcriptional and epigenetic programs of stem-like CD8$^+$ T cells. *Nat. Immunol.* **22**, 370–380 (2021).
32. Ataide, M. A. et al. BATF3 programs CD8$^+$ T cell memory. *Nat. Immunol.* **21**, 1397–1407 (2020).
33. Gasteiger, G., Fan, X., Dikiy, S., Lee, S. Y. & Rudensky, A. Y. Tissue residency of innate lymphoid cells in lymphoid and nonlymphoid organs. *Science* **350**, 981–985 (2015).
34. Huang, Y. et al. S1P-dependent interorgan trafficking of group 2 innate lymphoid cells supports host defense. *Science* **359**, 114–119 (2018).
35. Cortez, V. S. et al. Transforming growth factor-β signaling guides the differentiation of innate lymphoid cells in salivary glands. *Immunity* **44**, 1127–1139 (2016).
36. Tessmer, M. S., Reilly, E. C. & Brossay, L. Salivary gland NK cells are phenotypically and functionally unique. *PLoS Pathog.* **7**, e1001254 (2011).
37. Chiossone, L. et al. Maturation of mouse NK cells is a 4-stage developmental program. *Blood* **113**, 5488–5496 (2009).
38. Jeevan-Raj, B. et al. The transcription factor Tcf1 contributes to normal NK cell development and function by limiting the expression of granzymes. *Cell Rep.* **20**, 613–626 (2017).
39. Escobar, G., Mangani, D. & Anderson, A. C. T cell factor 1: a master regulator of the T cell response in disease. *Sci. Immunol.* **5**, eabb9726 (2020).
40. Oherle, K. et al. Insulin-like growth factor 1 supports a pulmonary niche that promotes type 3 innate lymphoid cell development in newborn lungs. *Immunity* **52**, 275–294.e279 (2020).
41. Collins, P. L. et al. Gene regulatory programs conferring phenotypic identities to human NK cells. *Cell* **176**, 348–360.e312 (2019).
42. Vieira Braga, F. A. et al. Blimp-1 homolog Hobit identifies effector-type lymphocytes in humans. *Eur. J. Immunol.* **45**, 2945–2958 (2015).
43. Behr, F. M. et al. Blimp-1 rather than hobit drives the formation of tissue-resident memory CD8$^+$ T cells in the lungs. *Front. Immunol.* **10**, 400 (2019).
44. Jansen, C. S. et al. An intra-tumoral niche maintains and differentiates stem-like CD8 T cells. *Nature* **576**, 465–470 (2019).
45. Krishna, S. et al. Stem-like CD8 T cells mediate response of adoptive cell immunotherapy against human cancer. *Science* **370**, 1328–1334 (2020).
46. Siddiqui, I. et al. Intratumoral Tcf1$^+$PD-1$^+$CD8$^+$ T cells with stem-like properties promote tumor control in response to vaccination and checkpoint blockade immunotherapy. *Immunity* **50**, 195–211 (2019).

Methods

Animals. B6 mice (C57BL/6), CD45.1 (B6.SJL-*Ptprc*^{a} *Pepc*^{b}/BoyJ), *Rag1*$^{-/-}$ (B6.129S7-*Rag1*^{tm1Mom}/J), *Rag2*$^{-/-}$*Il2rγ*$^{-/-}$(C;129S4-*Rag2*$^{tm1.1Flv}$ *Il2rg*$^{tm1.1Flv}$/J; herein referred to as *Rag2*$^{-/-}$*γc*$^{-/-}$), RORc-Cre (B6.FVB-Tg(Rorc-cre)1Litt/J), Ubi$^{Cre-ERT2}$ (B6.129-*Gt(ROSA)26Sor*$^{tm1(cre/ERT2)Tyj}$/J) and ROSA26–flox-stop-flox-eYFP (B6.129×1-*Gt(ROSA)26Sor*$^{tm1(EYFP)Cos}$/J) were originally purchased from The Jackson Laboratory. C57Bl/6NCr were purchased from Charles River. Hobit$^{Tom/KO}$ mice were generated by crossing B6-Tg(*Zfp683*-tdTomato-P2A-cre-P2A-DTR), here referred to as Hobit$^{Tom/WT}$ mice[17], with Hobit$^{KO/KO}$ mice[16]. NKp46^{iCre} (B6(Cg)-*Ncr1*$^{tm1.1(icre)Viv}$/Orl) mice[47] were generously provided by E. Vivier and crossed to Eomes$^{fl/fl}$ (ref. [48]) mice. FoxP3DTR (B6.129(Cg)-*Foxp3*$^{tm3(DTR/GFP)Ayr}$/J) mice were a gift from A. Rudensky[49]. All mice were bred and housed under specific-pathogen-free or germ-free conditions at the animal facility of the University Würzburg (Institute for Immunology and Virology, and Institute of Systems Immunology) and in the animal facility of the Netherlands cancer institute (NKI) in Amsterdam, and were used in accordance with institutional guidelines and as approved by the Lower Franconia government and the government of the Netherlands. Mice were kept in a 12-hour light–dark cycle, with an ambient temperature range within 20–24 °C; humidity ranged from 30–70%. For all experiments, male and female mice at 8–16 weeks of age were used.

Generation of Hobit^{KO} mice. To generate Hobit^{KO} mice, Zfp683$^{tm1a(KOMP)Wtsi}$ ES cell clones were obtained from the KOMP repository (www.komp.org) and generated by the Wellcome Trust Sanger Institute (WTSI) (see also Extended Data Fig. 3a)[50]. Mice were generated by Laser assisted (XY-Clone Hamilton Thorne) injection of JM8A3.N cells into 8-cell-stage C57Bl/6NCrl embryos. All injections were done with Narishige manipulators in the Transgenic Core Facility (TCF) of the MPI-CBG. Chimeras were crossed to C57Bl/6NCrl mice, and their offspring was screened by PCR for germline transmission. Hobit$^{fl/fl}$ mice were generated by breeding Hobit^{KO} mice with mice that express the Flp recombinase in the germ line[51]. Hobit$^{fl/fl}$ mice were crossed to Ubi$^{Cre-ERT2}$ mice[52].

Generation of mixed bone marrow chimeric mice. *Rag2*$^{-/-}$*γc*$^{-/-}$ mice were irradiated (3 Gy) and rested overnight. The next morning, bone marrow from femurs and tibias of CD45.2^{+} Hobit^{KO} and CD45.1^{+} WT mice was prepared and 5×10^{6} cells of each were intravenously injected into recipients.

Inducible deletion of Hobit by tamoxifen. For inducible deletion of Hobit, mice were treated intraperitoneally with 80 mg per kg (bodyweight) Tamoxifen (Sigma Aldrich) in corn oil (Sigma Aldrich) on day 0 and day 3. Mice were analyzed after 35–40 days of treatment.

In vivo T_{reg} cell depletion. To deplete T_{reg} cells, FoxP3^{DTR} mice were treated intraperitoneally with 200 µl 50 ng/g diphtheria toxin (DTx, Merck Millipore) in PBS or PBS only every other day. Mice were analyzed on day 8 after first treatment.

Tissue lymphocyte isolation. Mice were euthanized and perfused with PBS. For selected analyses, mice were intraperitoneally injected with 50 µg ARTC2.2 blocking nanobody s+16a (Biolegend) 30 min before euthanization to exclude the possibility that ILC viability was compromised through ARTC2-mediated NAD^{+}-induced cell death, but no difference to control groups was observed (data not shown). Livers, salivary glands, and kidneys were collected, cut into small pieces, and digested in DMEM (Gibco) with 10 mM Hepes (pH 7.2–7.5, Gibco), 20 µg/ml DNase I (Sigma Aldrich), and 1 mg/ml Collagenase D (Roche) at 37 °C and 100 r.p.m. for 40 min. Suspensions were passed through 100-µm filters and lymphocytes enriched by 40%/80% percoll (Sigma Aldrich) gradient (860*g*, 20 min, 21 °C, no breaks). The interface was washed with PBS (Sigma Aldrich) and used for flow cytometric analysis or sorting. Small intestine was collected, Peyer's patches were removed, and the intestine cut open longitudinally and washed extensively with PBS to remove feces. After dissociation using HBSS (Sigma Aldrich) supplemented with 5 mM EDTA (Carl Roth) and 10 mM Hepes (pH 7.2–7.5) at 37°C, tissues were cut into small pieces and digested in HBSS with 10 mM Hepes, 20 µg/ml DNase I, 0.5 mg/ml Collagenase D, and 50 U/ml Dispase (Corning) at 37 °C and 100 r.p.m. for 1 hour. Suspensions were passed through 100-µm filters and lymphocytes enriched by 40%/80% percoll (Sigma Aldrich) gradient (860*g*, 20 minutes, 21 °C, no breaks). The interface was washed with PBS (Sigma Aldrich) and used for flow cytometric analysis or sorting. mLN cell suspensions were filtered through 70-µm filters and used for flow cytometric analysis.

Flow cytometry and cell sorting. Dead cells were excluded by fixable viability dye eF780 (Thermo Fisher Scientific) and nonspecific binding blocked by anti-CD16/CD32 (BioXcell) blocking antibodies. Fluorochrome-conjugated monoclonal antibodies were purchased from commercial vendors (Supplementary Table 2).

For cell sorting of liver ILC1 and NK cells, single-cell suspensions were stained with FITC-labeled antibodies against CD5, CD19, F4/80, TCRβ, TCRγδ, and Ter119 and cells were negatively enriched using anti-FITC MicroBeads (Miltenyi), according to the manufacturer's recommendations. Cells were stained for CD45, NK1.1, CD3ε, CD49b, CD49a, IL-18R1, cKit, and biotinylated CD127, and subsequently with streptavidin. For cell sorting of SI ILC1, single-cell suspensions were stained with CD45, NK1.1, NKp46, CD90.2, CD127, CXCR6, and biotinylated CD3ε, CD5, CD19, F4/80, TCRβ, TCRγδ, and Ter119, and subsequently with streptavidin. When cells were sorted for scRNA-seq, hashtags and CITE-seq antibodies were included during this surface staining step. ILC1s were gated as live CD45^{+}Lin^{-}CD3ε^{-}NK1.1^{+}CD49b^{-}CD49a^{+} cells, and subsets were sorted based on CD127 and cKit. Sorting strategy for scRNA-seq is depicted in Extended Data Fig. 1. Cell sorting was performed on a BD FACSAria III.

For flow cytometry analysis, cells were stained with antibodies against CD11b, CD45, CD45.1, CD45.2, CD49a, CD49b, CD90.2, biotinylated and directly-conjugated CD127, CD160, CD200r, cKit, Cxcr6, Embigin, IL-18R1, NK1.1, NKp46, Sca-1, and TRAIL. Lineage-positive cells were stained with a cocktail of biotin-labeled antibodies against CD3ε, CD5, CD19, F4/80, FcεR1α, Ly6G, TCRβ, TCRγδ, and Ter119, followed by staining with streptavidin. Intracellular staining of CD3γ, CD127, Eomes, Gata-3, GM-CSF, Gzma, Gzmb, Gzmc, IFN-γ, TCF-1, TNF, Rorγt, and T-bet was performed using the FoxP3/Transcription Factor Staining Buffer set (Thermo Fisher Scientific). In some experiments, including all cultures of ILCs, CD127 BV421, or CD127 APC were used for intracellular staining of CD127, in order to detect CD127 when downregulated from the surface. For intracellular cytokine staining, cells were stimulated with 10 ng/ml IL-12 (Peprotech), 10 ng/ml IL-18 (RnD), and 1 µg/ml Brefeldin A (Sigma Aldrich) or with 50 ng/ml PMA (Sigma Aldrich), 500 ng/ml ionomycin (Sigma Aldrich), and 1 µg/ml Brefeldin A (Sigma Aldrich) in RPMI 1640 + GlutaMAX medium (Gibco) with 10% FCS (Sigma Aldrich) and 1× penicillin–streptomycin (Gibco) for 4 hours. Cells were acquired on a BD Celesta, BD FASSymphony cytometer using FACSDiva v9, or Cytek Aurora cytometer using SpectroFlo v2.2.0.2. Data were analyzed with FlowJo v9 and v10 software (BD). Unless otherwise indicated, ILC1s were gated as live CD45^{+}Lin^{-}NK1.1^{+}Eomes^{-}CD49a^{+} cells or CD45^{+}Lin^{-}NK1.1^{+}CD49b^{-}CD49a^{+} cells. NK cells were gated as live CD45^{+}Lin^{-}NK1.1^{+}Eomes^{+} cells or CD45^{+}Lin^{-}NK1.1^{+}CD49b^{+} (CD49a^{-}) cells. Small intestinal ILC1 were generally gated as live CD45^{+}Lin^{-}NKp46^{+}NK1.1^{+}Eomes^{-}RORγt^{-} cells or, to preserve the Hobit^{Tom} reporter signal, as live CD45^{+}Lin^{-}NKp46^{+}NK1.1^{+}CD90^{int}CD127^{+}Cxcr6^{+} cells (Extended Data Fig. 6a).

In vivo ILC1 cotransfer. CD127^{+} and CD127^{-} ILC1s were FACS-sorted from CD45.1 and CD45.1/CD45.2 congenic B6 mice and 5,000 cells of each were cotransferred intravenously into sublethally irradiated (3 Gy) CD45.2 *Rag2*$^{-/-}$*γc*$^{-/-}$ recipients. ILC1s were analyzed on day 15 post-transfer.

In vitro killing assay. FACS-sorted liver ILC1 subsets and NK cells were cultured at indicated ratios with 1,000 YAC1 cells. After 4 hours, absolute numbers of viable YAC1 cells were determined by FACS analysis and the percentage of specific killing was calculated compared with YAC1 cells cultured in the absence of ILCs or NK cells.

Culture of ILC1 and OP9 feeder cells. OP9, OP9-DL1, and OP9-DL4 feeder cells were grown at 5% CO2 in 1× MEM alpha (Gibco) supplemented with 20% FCS and 1× penicillin–streptomycin. At 80–90% confluence, cells were treated with 10 µg/ml mitomycin C (Sigma Aldrich) for 1.5 hours. Cells were washed three times with PBS and detached with trypsin–EDTA (Gibco) at 37 °C for 5 minutes, and 40,000 cells were seeded per well of a 96-well plate. Then, 400 FACS-sorted ILC1s were cultured on feeder cells at 5% CO_2 in RPMI 1640 with GlutaMAX medium supplemented with 10% FCS, 1× penicillin–streptomycin, 50 µM β-mercaptoethanol (Gibco) and 25 ng/ml murine IL-2 (Peprotech) or 25 ng/ml human IL-15 (Peprotech). After 7 days, cells were analyzed by flow cytometry. For analysis of cell proliferation, 2,000 FACS-sorted cells were labeled with Cell-Trace Violet (c34557; Invitrogen). Cells were stained in a 1.25 nM working solution in 1× PBS + 0.1 % (v/v) FCS and incubated in the dark for 20 minutes. Cells were washed 3 times with PBS and cultured on feeder cells at 5% CO_2 in RPMI 1640+ GlutaMAX medium supplemented with 10% FCS, 1× penicillin–streptomycin, 50 µM β-mercaptoethanol (Gibco), and 25 ng/ml murine IL-2 (Peprotech). After 4–8 days, cells were analyzed by flow cytometry.

scRNA-seq, cell hashing and CITE-seq. ILC1s and NK cells were sorted (as detailed above and in Supplementary Fig. 1) from Hobit$^{Tom/WT}$ and Hobit$^{Tom/KO}$ mice for scRNA-seq as four individual, hash-tagged populations before pooling into one reaction (TotalSeq-A0301 and TotalSeq-A0302, Biolegend). Hobit-deficient and sufficient ILC1s were pooled at similar ratios and enriched over NK cells to improve resolution of ILC1 subsets. Before sorting, cells were labeled with oligonucleotide-tagged antibodies targeting selected surface markers (CD11b, CD27, CD69, CD90.2, CD127, CD200r, NKp46; TotalSeq-A, Biolegend) for cellular indexing of transcriptomes and epitopes by sequencing (CITE-Seq)[53]. Immediately after sorting, the cells were encapsulated into droplets using 10x Genomics GemCode Technology (Single Cell 3′ Reagent kit v3) and processed following manufacturer's specifications for scRNA-seq library preparation. Three distinct libraries were generated: a CITE-Seq library, a Hashtag library, and the cDNA library fraction (corresponding to the cell transcriptome). Libraries were quantified by Qubit 3.0 Fluometer (Thermo Fisher), quality was checked using 2100 Bioanalyzer with the High-Sensitivity DNA kit (Agilent), and sequencing

was performed using a NovaSeq 6000 platform (Illumina) in 50-bp paired-end mode to reach approximately 150,000 reads per single cell. For adequate read coverage, we sequenced the CITE-seq library at 10%, the hashtag library at 5%, and the cDNA library fraction at 85% of a lane according to the manufacturer's recommendations (Biolegend). Data for the cDNA library fraction were demultiplexed using Cell Ranger software v3.0.2 (10x Genomics) and aligned to mouse mm10 reference genome.

Sample demultiplexing and doublet identification. To demultiplex hashtags, for each cell HTODemux function in Seurat package was used as described[54]. Cross-sample doublet cell detection was performed based on hashtag signal. Only cells that were classified as 'singlet' were retained and used for downstream analysis.

Clustering with Seurat. The datasets were analyzed using Seurat v3 standard workflow[55]. After log transformation with the command LogNormalize and scaling with ScaleData, basic QC has been performed. Viable cells have been selected by filtering for cells with UMI count superior at 1,000 and a percentage of UMI mapped to mitochondrial genes inferior to 8. Cells were then assigned to appropriate samples by demultiplexing the hashtags antibodies. Variable genes were identified by the function VariableFeatures with a *n* value of 2,000. Dimensions of the data were reduced first using a principal component analysis (PCA) on variable genes after removing genes that were identified as potential digestion-related stress signature, and then a uniform manifold approximation and projection (UMAP) on the 15 first PC dimensions. Cells were also assigned to clusters with the functions FindNeighbors on the same 15 PC dimensions and then FindClusters with a resolution of 0.7. Cluster specific gene signatures have been analyzed with the function FindAllMarkers from Seurat with arguments: only.pos = TRUE, min.pct = 0.25, logfc.threshold = 0.25. These markers were sorted by logFc and clusters to identify the top 30 cluster specific genes. Exhaustive list of marker defining cluster of interest have been generated with the Findmarkers function, with arguments: only.pos = TRUE, ident.1 = cluster of interest, ident.2 =NULL, logfc.threshold = 0.25, test.use = 'wilcox', min.pct = 0.1. Complete heatmap signature of ILC1 and NK has been generated by merging the outcome of Findmarkers function from the 3 different clusters and visualized with the DoHeatmap command from Seurat. In addition, ILC1 subsets were averaged with the Seurat function AverageExpression, and averaged object was plot as heatmap for described Hobit target genes.

Score calculation with Seurat. Scores were calculated for the current or for published dataset using the Seurat function AddModuleScore with default settings. An unbiased ILCP signature was derived by analysis of the Harly et al. dataset[29] following Seurat clustering analysis workflow and using the command FindAllMarkers on the dataset with default settings. Filtering the markers for adjusted $P < 0.01$, $\log_2$(fold change) > 1.5, and detection of transcript in at least 30% of cells in the cluster revealed the genes: *Ccl5*, *Lmo4*, *Rora*, *Il18r1*, *Id2*, *Tox2*, *Ltb*, *Gata3*, *Bcas1*, *Maf*, *Ikzf2*, *S100a4*, *Itgb3*, *Zbtb16*, *Ahcyl2*, *Pdcd1*, *Rxrg*, *Thy1*, and *Tox* markers of ILCP cluster. For the curated ILCP signature, we selected genes on the basis of different datasets and prior knowledge of ILCPs: *Runx3*, *Tox*, *Tox2*, *Tcf7*, *Lef1*, *Zbtb16*, *Gata3*, *Id2*, *Ikzf2*, *Rora*, *Lmo4*, *Rxrg*, *Maf*, *Bcl11b*, *Ikzf3*, *Batf3*, *Myb*, *Pdcd1*, *Kit*, *Il18r1*, and *Itgb3*.

Trajectory analysis with Slingshot. Trajectories were predicted using Slingshot 1.4.0 (ref. [56]) package. After subsetting the ILC1 population with the subset function, trajectory has been inferred using the function slingshot with a threshold of 0.05, a stretch of 2, and starting cluster 0. Variable genes have been visualized along pseudotime with the function plotGenePseudotime and as heatmap with the Pheatmap 1.0.12R package.

Clustering with RaceID3 and StemID2 analysis. The initial clustering was performed using VarID[57]. The following genes were removed and correlating gene groups in the filtering step (CGenes parameter): mitochondrial genes (mt*), ribosomal genes (Rpl*, Rps*), and predicted genes with Gm-identifiers (Gm*). Only cells with at least 1,000 transcripts were retained. VarID was run with no_cores = 1, alpha = 1, and default parameters otherwise. Prior to filtering and normalization, cells expressing > 2% of Kcnq1ot1 transcripts, identified as a marker of low-quality cells[27], were removed from the analysis. Differential gene expression analysis identified clusters with high expression of stress-response-related genes such as: heat-shock proteins (Hspa1a, Hspa1b) immediate early genes (IEGs) like Jun and Fos, Fosb (fold change values > 2). These clusters were removed from further analysis. Overall, 668 ILC1 WT (Cxcr6$^+$) cells passed the quality-control thresholds with a median of 6,578 transcripts and 2,245 different genes per cell. These cells were further analyzed using RaceID3 (ref. [58]). RaceID3 was run with the following parameters: mintotal = 1000, cln = 3, and default parameters otherwise. CGenes parameter was initialized for the same genes as described above for VarID.

For derivation of differentiation trajectories the StemID2 algorithm was used[27,58]. StemID2 was run on the clusters obtained from RaceID3 with the following parameters: cthr = 5, pthr = 0.05, nmode = TRUE, um = TRUE. Self-organizing maps (SOMs) were used to infer models of pseudotemporal expression profiles using the following parameters: nb = 200, alpha = 0.8, corthr = 0.85, minsom = 3.

Statistical analysis. All experiments were performed using randomly assigned mice. No statistical methods were used to predetermine sample sizes. Sample sizes were chosen on the basis of our previous experiences with similar analyses. Data distribution was assumed to be normal but this was not formally tested. Statistical significance was calculated by unpaired two-tailed *t*-test: $^*P < 0.05$, $^{**}P < 0.01$, $^{***}P < 0.001$, $^{****}P < 0.0001$. All statistical analysis were performed with Prism 7 (GraphPad Software). Bar graphs indicate individual mice (symbols) and mean (bar), error bars display means ± s.d.

Reporting Summary. Further information on research design is available in the Nature Research Reporting Summary linked to this article.

Data availability

The sequencing data that were generated for this report have been deposited in Gene Expression Omnibus under the accession number GSE163452. An interactive online resource of single cell sequencing analyses is available on https://go.uniwue.de/hobit. Sequencing data for ILCP analysis was recently published by Harly et al.[29]. Source data are provided with this paper in the Supplementary File. Source data are provided with this paper.

References

47. Narni-Mancinelli, E. et al. Fate mapping analysis of lymphoid cells expressing the NKp46 cell surface receptor. *Proc. Natl Acad. Sci. USA* **108**, 18324–18329 (2011).
48. Zhu, Y. et al. T-bet and eomesodermin are required for T cell-mediated antitumor immune responses. *J. Immunol.* **185**, 3174–3183 (2010).
49. Kim, J. M., Rasmussen, J. P. & Rudensky, A. Y. Regulatory T cells prevent catastrophic autoimmunity throughout the lifespan of mice. *Nat. Immunol.* **8**, 191–197 (2007).
50. Skarnes, W. C. et al. A conditional knockout resource for the genome-wide study of mouse gene function. *Nature* **474**, 337–342 (2011).
51. Kranz, A. et al. An improved Flp deleter mouse in C57Bl/6 based on Flpo recombinase. *Genesis* **48**, 512–520 (2010).
52. Ventura, A. et al. Restoration of p53 function leads to tumour regression in vivo. *Nature* **445**, 661–665 (2007).
53. Stoeckius, M. et al. Simultaneous epitope and transcriptome measurement in single cells. *Nat. Methods* **14**, 865–868 (2017).
54. Stoeckius, M. et al. Cell hashing with barcoded antibodies enables multiplexing and doublet detection for single cell genomics. *Genome Biol.* **19**, 224 (2018).
55. Stuart, T. et al. Comprehensive integration of single-cell data. *Cell* **177**, 1888–1902 (2019).
56. Street, K. et al. Slingshot: cell lineage and pseudotime inference for single-cell transcriptomics. *BMC Genomics* **19**, 477 (2018).
57. Grün, D. Revealing dynamics of gene expression variability in cell state space. *Nat. Methods* **17**, 45–49 (2020).
58. Herman, J. S., Sagar & Grün, D. FateID infers cell fate bias in multipotent progenitors from single-cell RNA-seq data. *Nat. Methods* **15**, 379–386 (2018).

Acknowledgements

We thank C. Romagnani for critically reading the manuscript, and S. Klingler, M. Lian, S. Riedmann, L. Parga-Vidal and the IZKF FACS sorting facility Würzburg for expert technical assistance. We thank E. Vivier (Aix Marseille Univ., CNRS, INSERM, CIML, Marseille, France) and A. Rudensky (Howard Hughes Medical Institute, Immunology Program, and Ludwig Center, Memorial Sloan Kettering Cancer Center, New York, USA) for providing mice. We thank R. Naumann (MPI-CBG, Dresden) for providing Flp deleter mice and for microinjections of Hobit^{KO} ES cells. This work was supported by grants through the German Research Foundation (DFG) priority program SPP1937 – Innate lymphoid cells (GA2129/2-2 to G.Gasteiger and GR4980/1-2 to D.G.), through the European Research Council (759176-TissueLymphoContexts to G.Gasteiger, 818846-ImmuNiche to D.G. and 819329- STEP2 to W.K.). G.Gasteiger and D.G. are supported by the Max Planck Society. P.A. acknowledges financial support from Interdisciplinary Center for Clinical Research-IZKF (project Z-6). A.-E.S. is supported by the EMBO Young Investigator program. K.P.J.M.v.G. was funded by a LSBR fellowship from Landsteiner Foundation of Blood Transfusion Research (1629).

Author contributions

G.Gasteiger and K.P.J.M.v.G. conceptualized the study, provided funding, and coordinated the project. G.Gasteiger, K.P.J.M.v.G. and C.F. wrote the manuscript with input from all authors. C.F., R.L.R.E.T., R.M. and N.A.M.K. planned and performed experiments and analyzed the data. P.A. and A.-E.S. performed scRNA-seq. R.-D.L., and G.Golda analyzed scRNA-seq experiments. M.G.d.A. and K.K. provided critical reagents. W.K. and D.G. provided intellectual input and conceptual advice.

Competing interests

K.K. is an employee of Morphosys AG and former employee of the Roche Innovation Center Munich.

Additional information

Extended data is available for this paper at https://doi.org/10.1038/s41590-021-01013-0.

Supplementary information The online version contains supplementary material available at https://doi.org/10.1038/s41590-021-01013-0.

Correspondence and requests for materials should be addressed to G.G.

Peer review information *Nature Immunology* thanks the anonymous reviewers for their contribution to the peer review of this work. L. A. Dempsey was the primary editor on this article and managed its editorial process and peer review in collaboration with the rest of the editorial team.

Reprints and permissions information is available at www.nature.com/reprints.

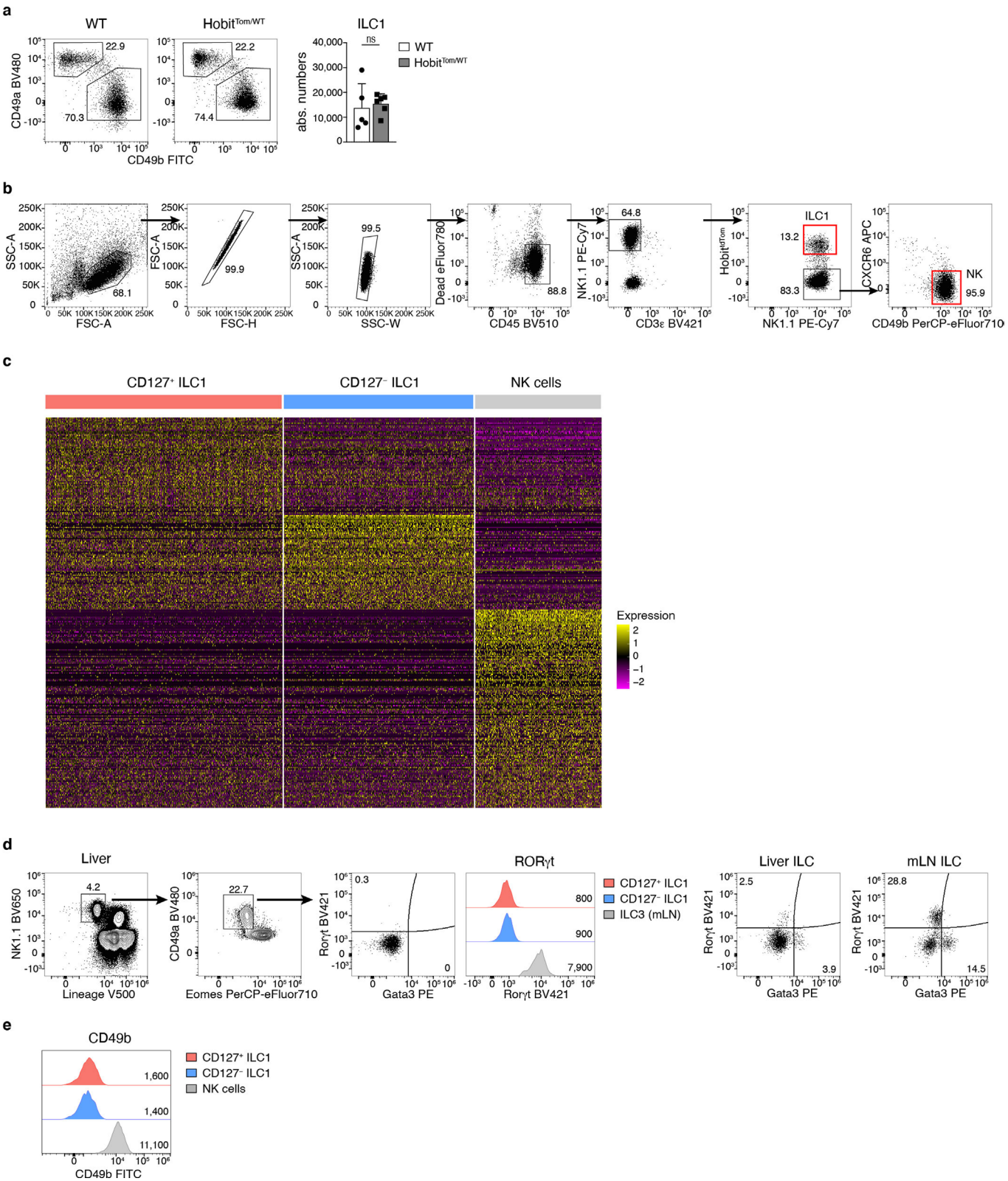

Extended Data Fig. 1 | Characterization of hepatic group 1 ILCs and gating strategy. a Representative FACS plots display Lin⁻NK1.1⁺ cells of WT and Hobit$^{Tom/WT}$ mice. Bar graphs indicate absolute numbers of liver ILC1s. Data are pooled from 2 independent experiments with n=2 and 3 mice per group. **b** Full sorting strategy for liver ILC1 and NK cells from negatively enriched liver lymphocytes of Hobit$^{Tom/WT}$ mice. **c** Heat map overview of significantly differentially expressed genes of ILC1 and NK cell clusters from Fig. 1c using Seurat. **d, e** Gating strategy to identify Lin⁻ NK1.1⁺ Eomes⁻ CD49a⁺ liver ILC1 and histograms showing Gata3, RORγt (d) and CD49b (e) protein expression within liver ILC1. Liver and mesenteric lymph nodes are gated on Lin⁻CD127⁺ cells to display Gata3 and RORyt expression. Data are representative of 2 individual experiments with n=3 mice. Bar graphs indicate individual mice (symbols) and mean (bar), error bars display means ± SD. Statistical significance was calculated by unpaired two-tailed *t*-test.

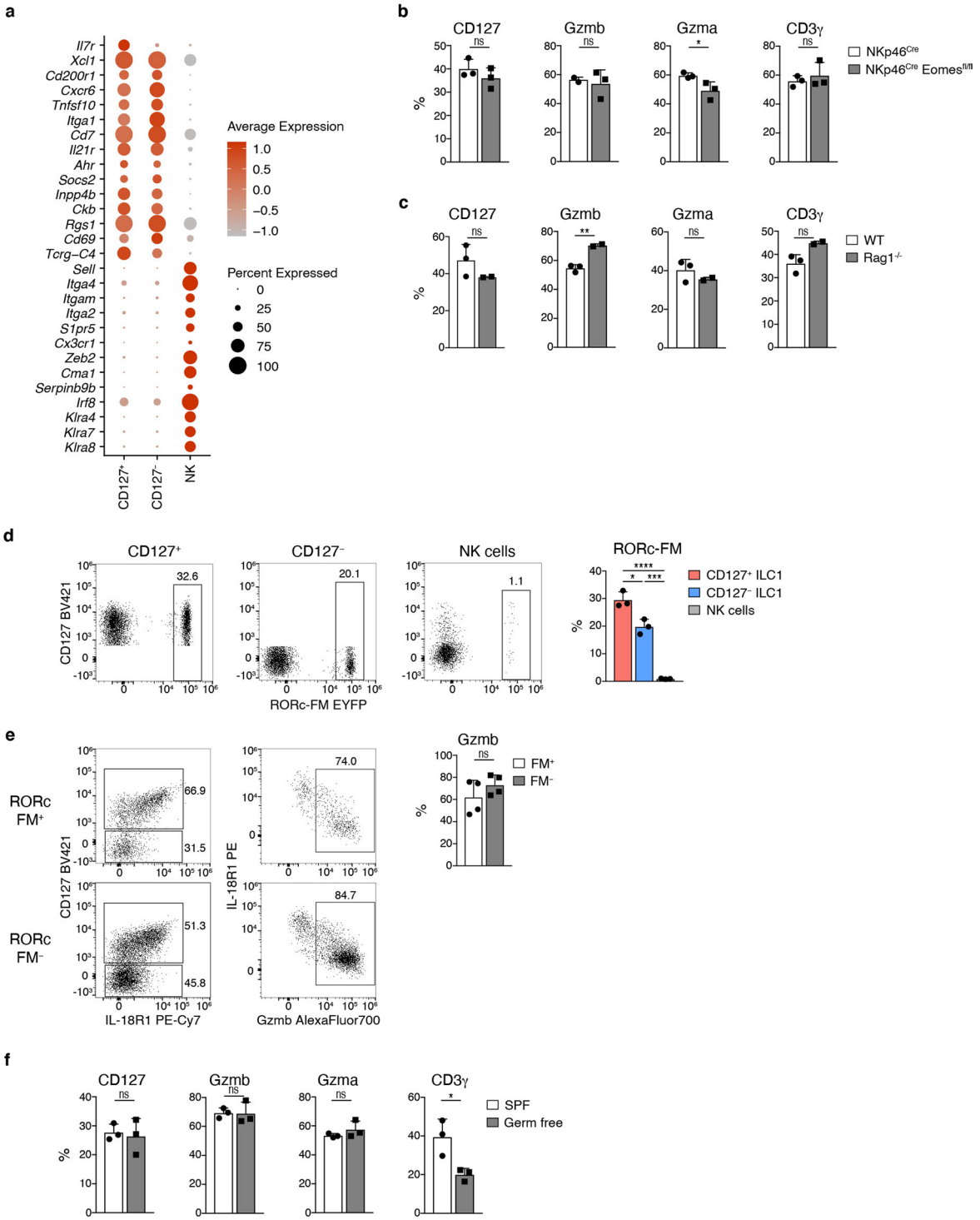

Extended Data Fig. 2 | CD127⁻ cytotoxic-like cells are bona-fide ILC1s. a Dot plot representation of selected ILC1 and NK cell marker gene expression associated with the clusters identified in Fig. 1c. Color indicates z-score of mean expression across clusters and dot size represents fraction of cells in the cluster expressing the respective gene. **b, c, f** Frequency of liver ILC1s expressing indicated proteins in NKp46^{Cre} versus NKp46^{Cre} Eomes$^{fl/fl}$ mice (**b**), WT versus *Rag1*$^{-/-}$ mice (**c**) and SPF versus germ free mice (**f**). Data are representative of 2 independent experiments with n=2 and 3 mice per group (**b, c, f**). **d, e** Representative FACS analysis of liver ILC1 of RORc-eYFP fate mapper (FM) mice. (**d**) FACS analysis and bar graph shows frequency of RORc fate map-positive cells within CD127⁺ and CD127⁻ liver ILC1 and NK cells. Data are representative of 2 independent experiments with n=3 mice per group. (**e**) FACS plots show marker protein expression of RORc fate mapper-positive (top) and negative (bottom) liver ILC1s. Bar graphs show frequency of Gzmb-positive cells within FM-positive and FM-negative ILC1s. Data are pooled from 2 independent experiments with n=2 mice per group. Bar graphs indicate individual mice (symbols) and mean (bar), error bars display means ± s.d. Statistical significance was calculated by unpaired two-tailed *t*-test; $^{*}P < 0.05$, $^{**}P < 0.01$, $^{***}P < 0.001$, $^{****}P < 0.0001$.

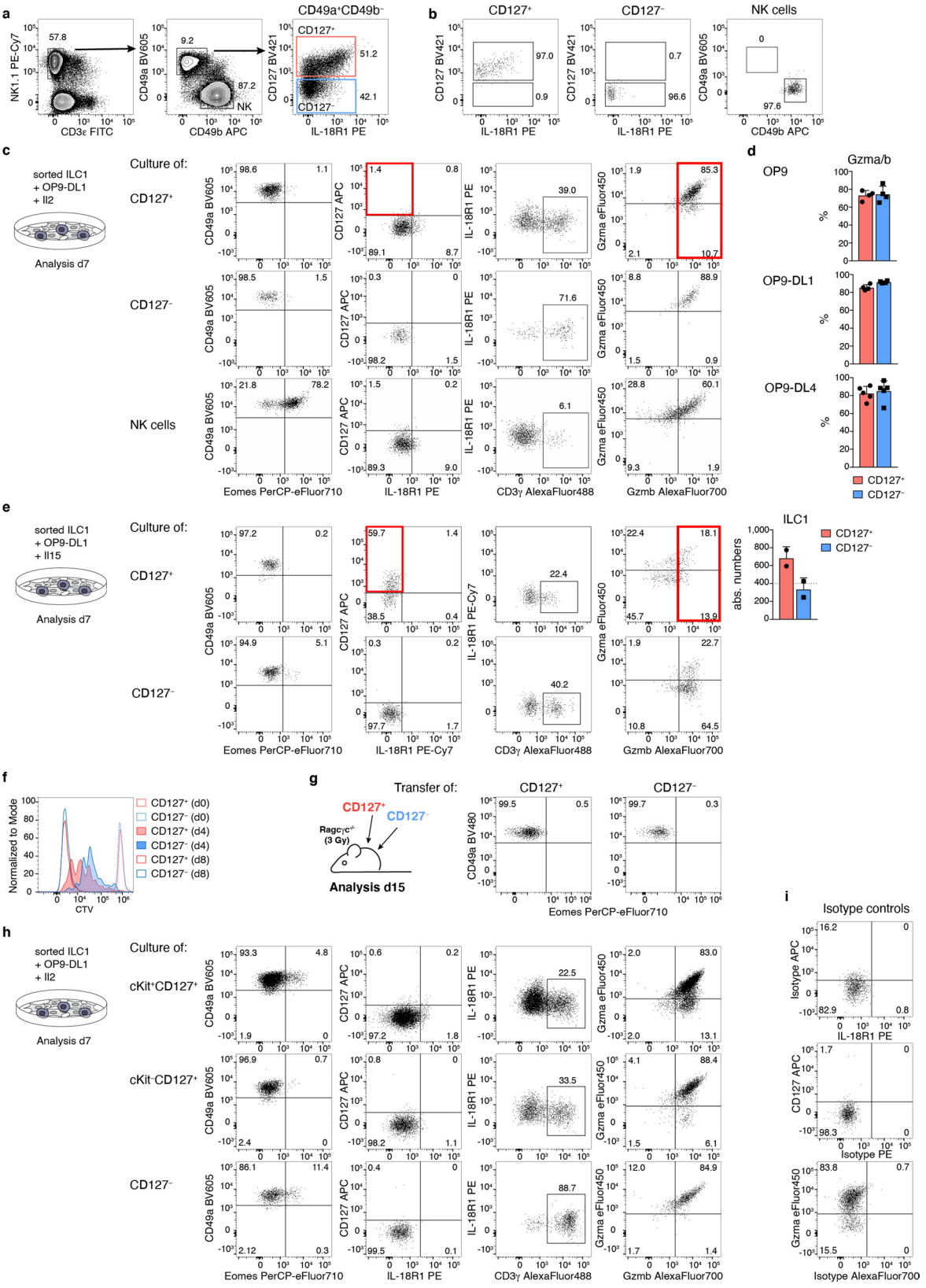

Extended Data Fig. 3 | See next page for caption.

Extended Data Fig. 3 | CD127$^+$ ILC1s give rise to CD127$^-$ cytotoxic-like ILC1s in vitro and in vivo. a, b Sorting strategy for CD127$^+$ and CD127$^-$ liver ILC1 and NK cells from WT mice, gated on live CD45$^+$ cells. **b** Sorting purity. **c-f, h, i** *In vitro* cultures of indicated liver ILC1 subsets with IL-2 (**c, d, f, h, i**) or IL-15 (**e**) and OP9-DL1 cells (**c, e, h, i**) or the indicated stromal cell line (**d**) for 7 days. Representative FACS analysis showing phenotype of NK1.1$^+$ cells. Red quadrants on FACS plots highlight phenotypic differences of CD127$^+$ ILC1 cultured in the presence of IL-2 versus IL-15. **d** Frequency of Gzma$^+$Gzmb$^+$ cells on day 7. **e** Absolute numbers on d7. Dashed line indicates number of cells on d0 (input=400 cells). **f** *In vitro* proliferation of ILC1 subsets assessed by cell tracer violet dilution analyzed on the indicated days. Data are representative of 2 independent experiments with n=4 and 5 (**d**), n=2 (**e**), n=4 (**f**) replicates per experiment. **g** *In vivo* co-transfer of congenically marked CD127$^+$ and CD127$^-$ liver ILC1s into sublethally irradiated *Rag2*$^{-/-}\gamma c^{-/-}$ mice. Representative FACS analysis of liver ILC1s derived from indicated transferred ILC1 subsets on d15. **i** Isotype control stainings of ILC1s cultured *in vitro* as in h. Bar graphs indicate replicates (symbols) and mean (bar), error bars display means ± s.d.

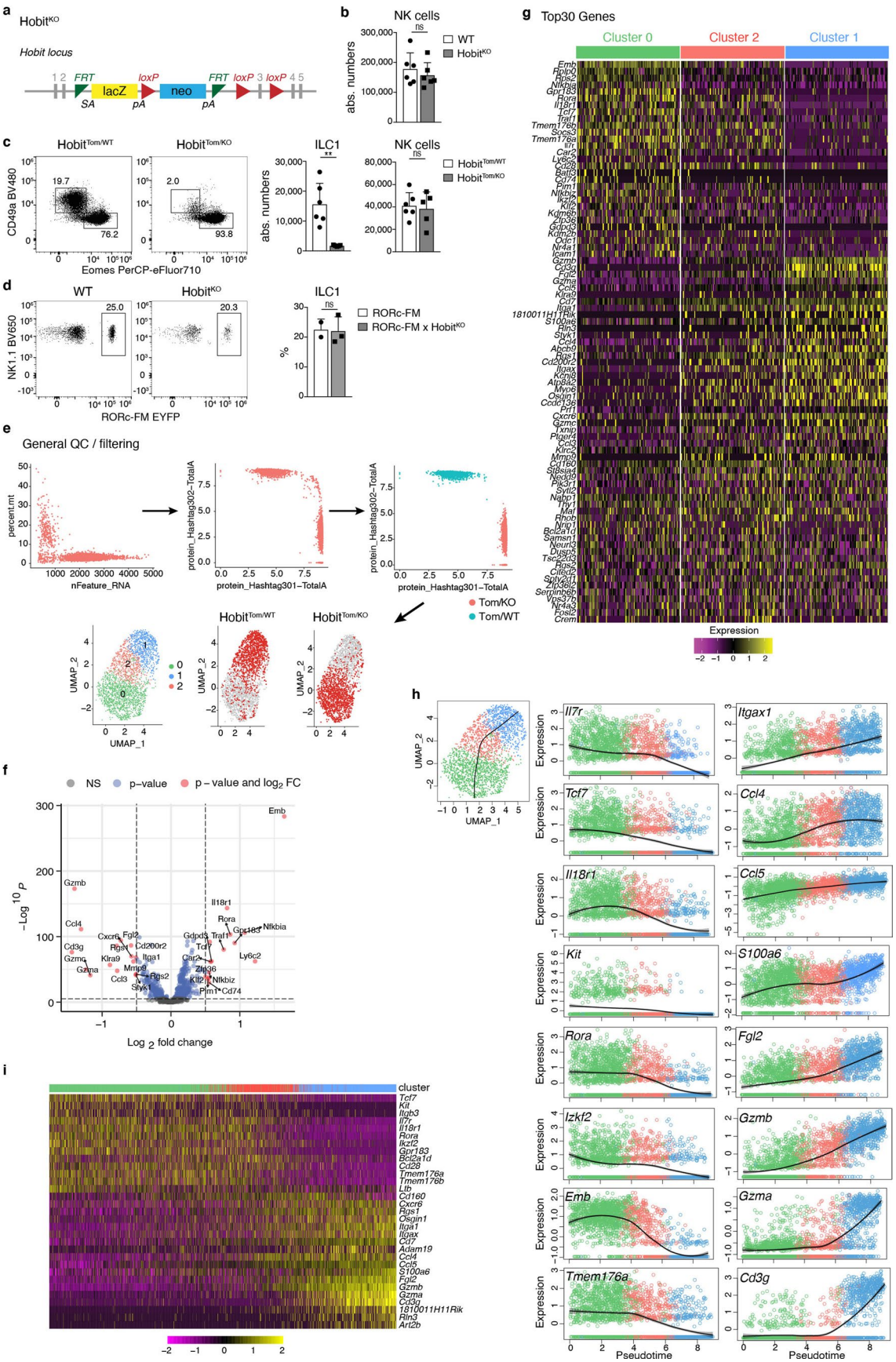

Extended Data Fig. 4 | See next page for caption.

Extended Data Fig. 4 | scRNA-seq analysis of hepatic ILC1s from WT and Hobit^{KO} mice. a Schematic representation of the *Hobit* locus of Hobit ^{KO} mice. **b** Absolute numbers of liver NK cells of WT and Hobit^{KO} mice. **c** Representative FACS analysis displaying Lin$^-$NK1.1$^+$ hepatic ILC1s and NK cells in Hobit$^{Tom/WT}$ and Hobit$^{Tom/KO}$ mice. Bar graphs indicate absolute numbers of liver ILC1s. Data in (**b**) and (**c**) are pooled from 2 independent experiments with n=3 (**b**) and n=2 and 3 (**c**) mice per group. **d** Representative FACS analysis of liver ILC1s of Hobit^{KO} RORc-eYFP fate mapper (FM) mice. Bar graph shows frequency of RORc fate map-positive cells within CD127$^+$ and CD127$^-$ liver ILC1s. Data are representative of 2 independent experiments with n=2-3 mice per group. **e-g** scRNA-seq of hash-tagged liver ILC1 sorted from Hobit$^{Tom/WT}$ and Hobit$^{Tom/KO}$ mice. **e** General QC, low quality cells (feature counts > 1000 and percentage of genes mapped to mitochondrial genome < 8) and cell doublets filtering and demultiplexing of Hashtag (HT) antibodies allows to separate Hobit$^{KO/Tom}$ (KO) and Hobit$^{Tom/WT}$ (WT). Single cell transcriptome visualization using a UMAP color-coded by clusters and the sample WT or KO as indicated by the binary detection of the HT antibodies. **f** Volcano plot displaying significantly differentially expressed genes between WT and Hobit^{KO} ILC1, using Wilcoxon test. Thresholds are displayed at Log2 FC equal 0.5 and Adjusted P value of 0.05. Genes on the right are overexpressed in KO, genes on the left are overexpressed in WT. **g** Heat map of marker gene expression differentially expressed across liver ILC1s. Cluster number refers to panel (**e**). **h, i** Pseudo-temporal ordering of ILC1 single cell transcriptomes with Slingshot. Expression of candidate genes across pseudotime within hash-tagged liver ILC1s sorted from Hobit$^{Tom/WT}$ and Hobit$^{Tom/KO}$ mice. Color barcode in (**h**) indicates cluster identity (as identified in **e**). Heatmap of expression of selected genes in ILC1 populations along pseudotime (**i**). Bar graphs indicate individual mice (symbols) and mean (bar), error bars display means ± s.d. Statistical significance was calculated by unpaired two-tailed *t*-test; $^{**}P < 0.01$.

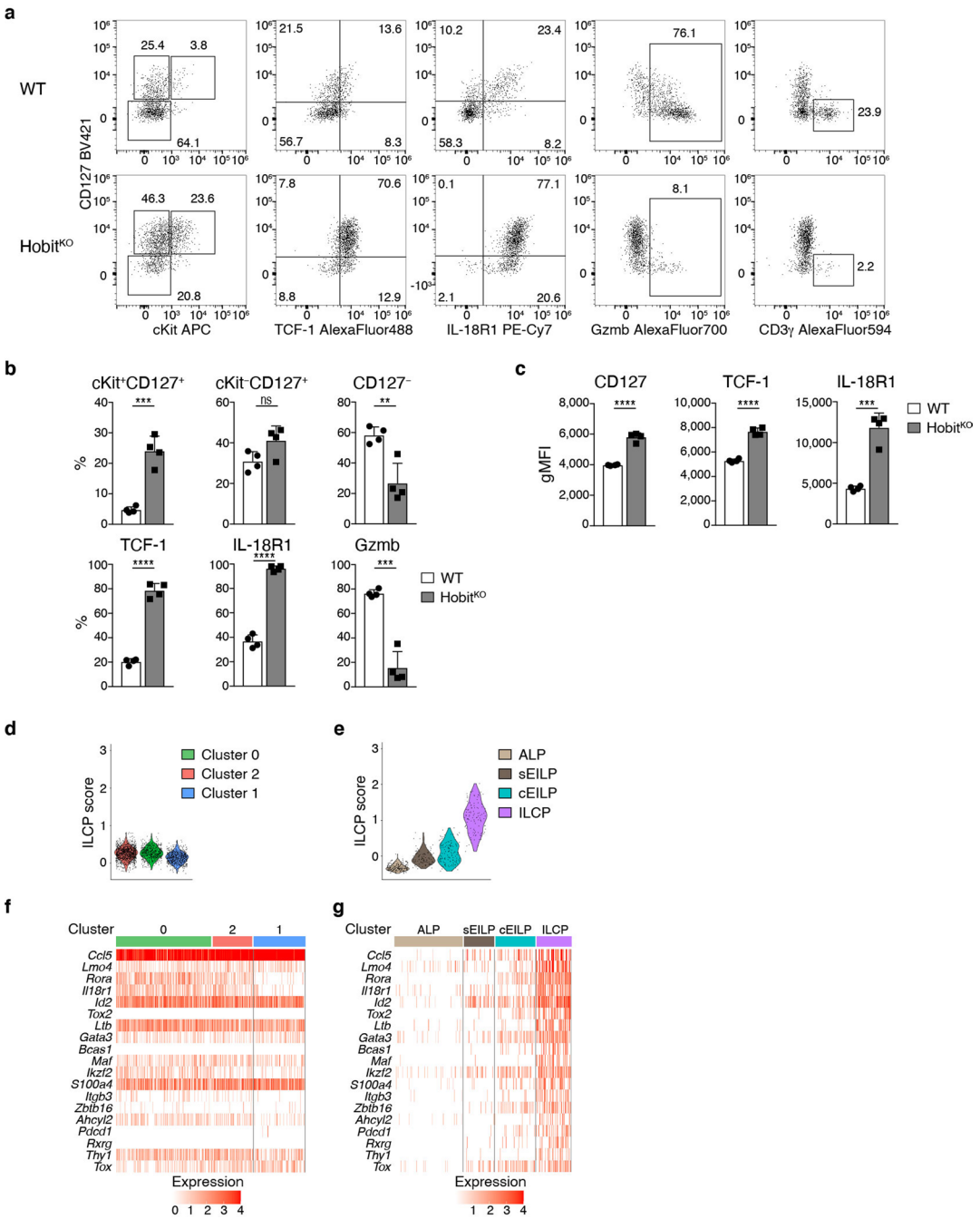

Extended Data Fig. 5 | Hobit drives the development and effector maturation of hepatic ILC1s and is expressed in committed ILC1s. a-c Representative FACS analysis of liver ILC1s in mixed bone marrow chimeric mice containing a congenically marked WT and Hobit^{KO} compartment (**a**). Frequency of liver ILC1 expressing indicated marker (**b**) and gMFI of CD127, TCF-1 and IL-18R1 expression within the respective marker-positive cells (**c**). Data are representative of 3 individual experiments with n=4 mice per group (**a-c**). **d-g** Analysis of an unbiased ILCP core signature derived from a scRNA-seq dataset of M progenitors generated by Harly *et al*[29]. Violin plots display ILCP score calculation and heat maps display individual gene expression across identified clusters (**d, f**) and in the dataset generated by Harly *et al*[29](**e, g**). ALP - all-lymphoid progenitors, sEILP - specific early innate lymphoid progenitors, cEILP - committed early innate lymphoid progenitors, ILCP - innate lymphoid progenitors. Bar graphs indicate individual mice (symbols) and mean (bar), error bars display means ± s.d. Statistical significance was calculated by unpaired two-tailed *t*-test; $^{**}P < 0.01$, $^{***}P < 0.001$, $^{****}P < 0.0001$.

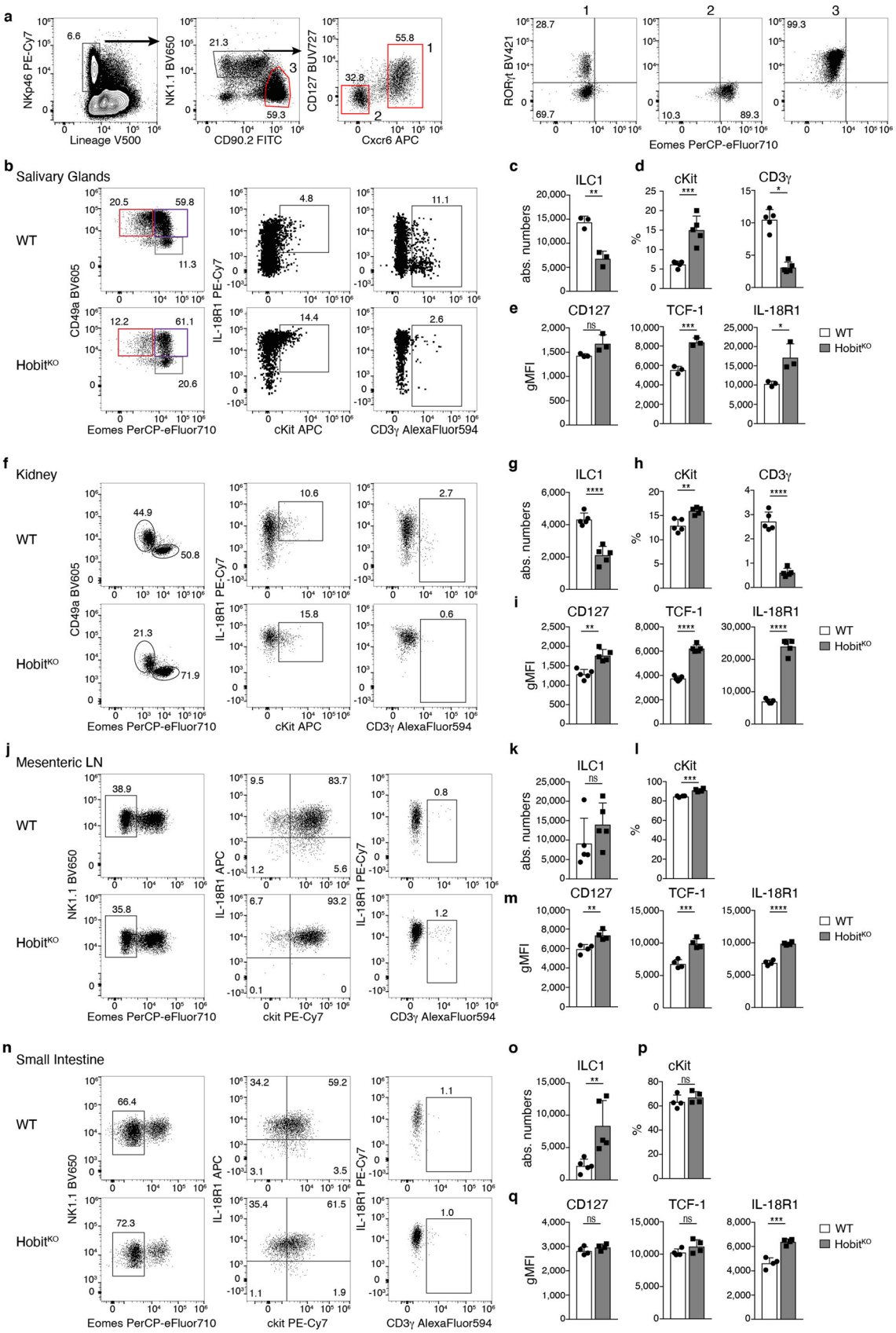

Extended Data Fig. 6 | See next page for caption.

Extended Data Fig. 6 | Effector differentiation of ILC1s is regulated by Hobit across tissues. a Gating strategy identifying ILC1s among live CD45$^+$ cells in the small intestine lamina propria for data depicted in Fig. 7a. To preserve the Hobit^{Tom} signal, cells were gated without transcription factor staining. ILC1 (1) were enriched as Lin$^-$ NKp46$^+$ NK1.1^{hi}CD90^{int} CXCR6$^+$ CD127$^+$ cells, NK cells (2) were gated as Lin$^-$ NKp46$^+$ NK1.1^{hi} CD90^{int} CXCR6$^-$ CD127$^-$ cells, NKp46$^+$ ILC3 were gated as Lin$^-$ NKp46$^+$ CD90^{hi} cells. Purity of gating strategy is displayed by analysis of RORγt and Eomes (right). **b-q** Analysis of ILC1 in salivary glands (**b-e**), kidneys (**f-i**), mesenteric lymph nodes (**j-m**) and small intestine lamina propria (**n-q**). **b, f, j, n** Representative FACS analysis of Lin$^-$NK1.1$^+$ cells (left row of FACS plots) and Eomes$^-$CD49a$^+$ ILC1s (middle and right row) of WT and Hobit^{KO} mice. **b** Representative FACS plot identifying ILC1 (Eomes$^-$CD49a$^+$), Eomes$^+$CD49a$^+$NK1.1$^+$ cells (Eomes$^+$CD49a$^+$) and cNK cells (Eomes$^+$CD49a$^-$) within Lin$^-$NK1.1$^+$ cells (left panel). **c, g, k, o** Bar graphs indicate absolute numbers of ILC1. **d, h, l, p** Frequency of ILC1s expressing indicated marker proteins. **e, i, m, q** gMFI of CD127, TCF-1 and IL-18R1 expression within ILC1 that are gated as positive for the respective marker. Data are representative of 3 independent experiments with n=3 (**c, e**), n=4 (**j, l, m, p, q**) and n=5 (b, d, f-i, k, o) mice per group. Bar graphs indicate individual mice (symbols) and mean (bar), error bars display means ± s.d. Statistical significance was calculated by unpaired two-tailed *t*-test; *P < 0.05, ***P* < 0.01, ****P* < 0.001, *****P* < 0.0001.

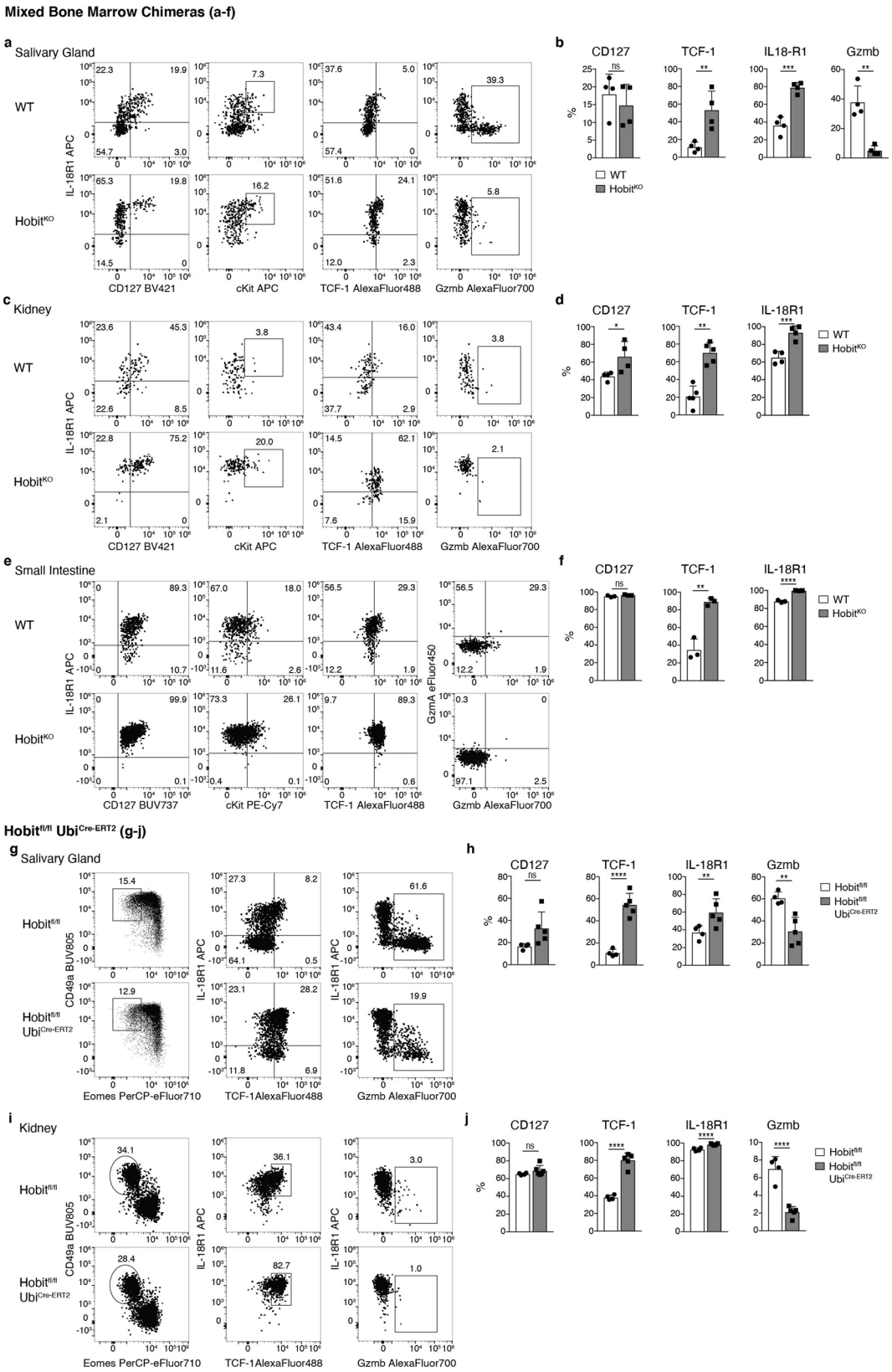

Extended Data Fig. 7 | Analysis of ILC1s in mixed bone marrow chimeric mice and upon inducible deletion of Hobit. Representative FACS analysis of ILC1s in salivary glands (**a, b, g, h**), kidneys (**c, d, i, j**) and small intestine lamina propria (**e, f**) of mixed bone marrow chimeric mice (**a-f**) or Ubi$^{Cre\text{-}ERT2}$ Hobit$^{fl/fl}$ mice and littermate controls on d35 after Tamoxifen treatment (**g-j**). Bar graphs indicate frequency of ILC1s expressing indicated proteins. Data are representative of 2 (**e, f**) or 3 (**a-d, g-j**) individual experiments with n=3 (**f**), n=4 (**a-d, g-j**) and n=5 (**d, h, j**) mice per group. Bar graphs indicate individual mice (symbols) and mean (bar), error bars display means ± s.d. Statistical significance was calculated by unpaired two-tailed *t*-test; $^{*}P < 0.05$, $^{**}P < 0.01$, $^{***}P < 0.001$, $^{****}P < 0.0001$.

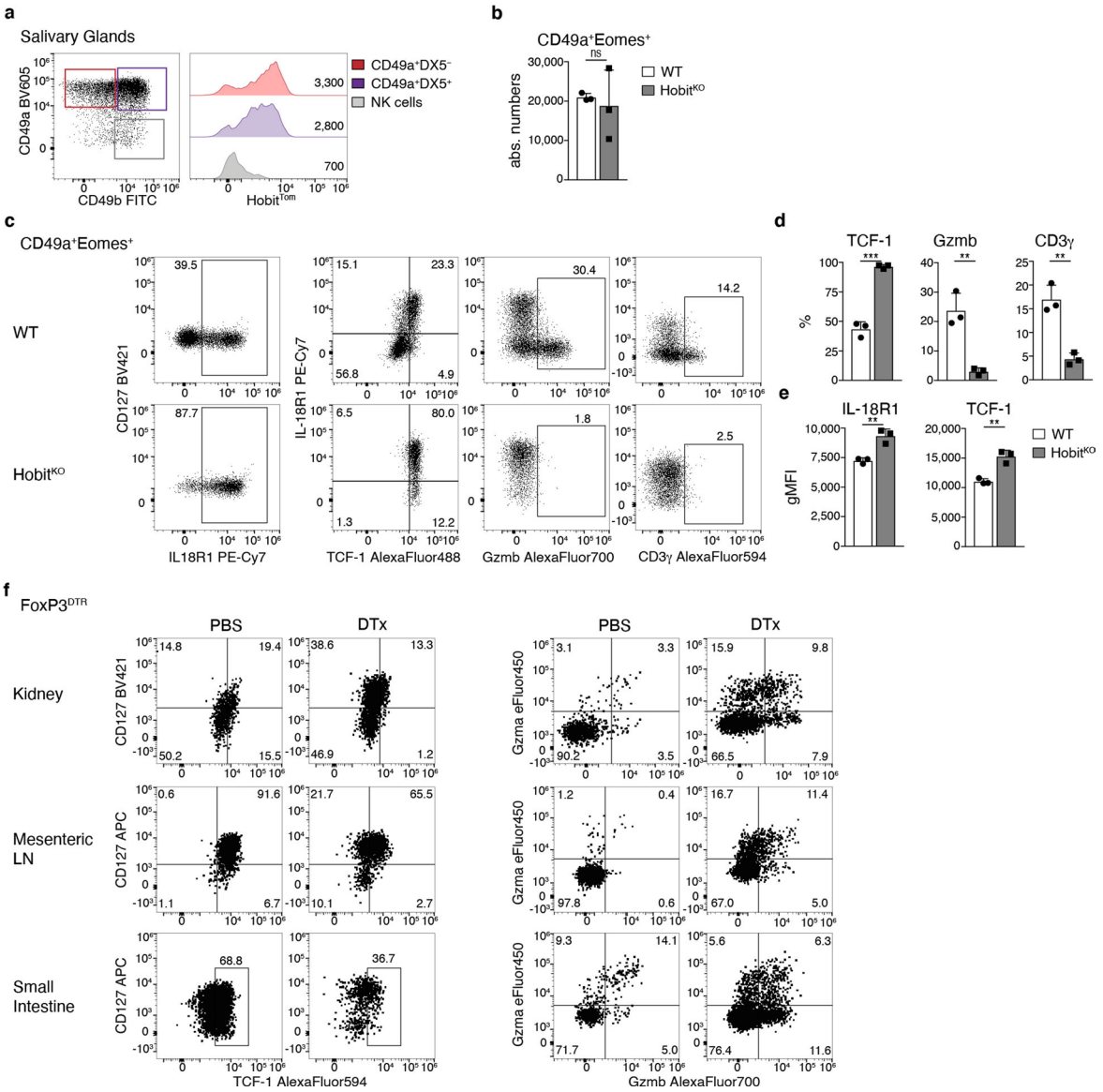

Extended Data Fig. 8 | Hobit regulates the effector differentiation of Eomes$^+$CD49a$^+$ group 1 ILCs, and phenotype of ILC1s in Treg cell-depleted mice. **a-e** FACS analysis of Eomes$^+$CD49a$^+$ tissue-resident NK1.1$^+$ cells in salivary glands of WT and Hobit^{KO} mice. **a** Representative FACS analysis of Hobit^{Tom} expression within ILC1 (CD49b$^-$CD49a$^+$), Eomes$^+$CD49a$^+$NK1.1$^+$ cells (identified by gating as CD49b$^+$CD49a$^+$, to avoid permeabilization for the analysis of the Hobit^{Tom} reporter signal) and cNK cells (CD49b$^+$CD49a$^-$) within Lin$^-$NK1.1$^+$ cells. **b** Absolute numbers of Eomes$^+$CD49a$^+$NK1.1$^+$ cells. **c** Representative FACS analysis showing indicated marker expression. **d** Frequency of marker-positive cells. **e** gMFI of TCF-1 and IL-18R1 expression within marker-positive cells. Data are representative of 3 independent experiments with n=3 mice per group. **f** Representative FACS plots show expression of indicated proteins of ILC1s in kidneys, mesenteric lymph nodes and small intestine lamina propria of FoxP3^{DTR} mice on d8 of Treg cell depletion (DTx). Data are representative of 2-3 independent experiments with n=4 mice per group. Bar graphs indicate individual mice (symbols) and mean (bar), error bars display means ± s.d. Statistical significance was calculated by unpaired two-tailed *t*-test; $^{**}P < 0.01$, $^{***}P < 0.001$.

nature research

Corresponding author(s): Georg Gasteiger

Last updated by author(s): Jul 28, 2021

Reporting Summary

Nature Research wishes to improve the reproducibility of the work that we publish. This form provides structure for consistency and transparency in reporting. For further information on Nature Research policies, see our Editorial Policies and the Editorial Policy Checklist.

Statistics

For all statistical analyses, confirm that the following items are present in the figure legend, table legend, main text, or Methods section.

n/a	Confirmed	
☐	☒	The exact sample size (*n*) for each experimental group/condition, given as a discrete number and unit of measurement
☐	☒	A statement on whether measurements were taken from distinct samples or whether the same sample was measured repeatedly
☐	☒	The statistical test(s) used AND whether they are one- or two-sided *Only common tests should be described solely by name; describe more complex techniques in the Methods section.*
☒	☐	A description of all covariates tested
☒	☐	A description of any assumptions or corrections, such as tests of normality and adjustment for multiple comparisons
☐	☒	A full description of the statistical parameters including central tendency (e.g. means) or other basic estimates (e.g. regression coefficient) AND variation (e.g. standard deviation) or associated estimates of uncertainty (e.g. confidence intervals)
☐	☒	For null hypothesis testing, the test statistic (e.g. *F*, *t*, *r*) with confidence intervals, effect sizes, degrees of freedom and *P* value noted *Give P values as exact values whenever suitable.*
☒	☐	For Bayesian analysis, information on the choice of priors and Markov chain Monte Carlo settings
☒	☐	For hierarchical and complex designs, identification of the appropriate level for tests and full reporting of outcomes
☒	☐	Estimates of effect sizes (e.g. Cohen's *d*, Pearson's *r*), indicating how they were calculated

Our web collection on statistics for biologists contains articles on many of the points above.

Software and code

Policy information about availability of computer code

Data collection	FACSDiva v9, SpectroFlo v2.2.0.2, Cell Ranger v3.0.2
Data analysis	FlowJo v9 and v10 for FACS data analysis GraphPad Prism v7 for statistical analysis Seurat v3, Slingshot v1.4.0, Pheatmap v1.0.12 R package, VarID v0.2.3, RaceID3, StemID2 for scRNA-Seq Analysis.

For manuscripts utilizing custom algorithms or software that are central to the research but not yet described in published literature, software must be made available to editors and reviewers. We strongly encourage code deposition in a community repository (e.g. GitHub). See the Nature Research guidelines for submitting code & software for further information.

Data

Policy information about availability of data

All manuscripts must include a data availability statement. This statement should provide the following information, where applicable:

- Accession codes, unique identifiers, or web links for publicly available datasets
- A list of figures that have associated raw data
- A description of any restrictions on data availability

The sequencing data that were generated for this report have been deposited in Gene Expression Omnibus under the accession number GSE163452. Single cell sequencing analyses are also available on https://go.uniwue.de/hobit. Sequencing data for ILCP analysis was recently published by Harly et al., Nature Immunology 2019, GSE xxx. Source data are provided with this paper in the Supplementary File.

Field-specific reporting

Please select the one below that is the best fit for your research. If you are not sure, read the appropriate sections before making your selection.

☒ Life sciences ☐ Behavioural & social sciences ☐ Ecological, evolutionary & environmental sciences

For a reference copy of the document with all sections, see nature.com/documents/nr-reporting-summary-flat.pdf

Life sciences study design

All studies must disclose on these points even when the disclosure is negative.

Sample size	No statistical methods were used to pre-determine sample sizes; sample sizes were chosen based on our previous experiences with similar analyses (Zeis et al.). For all in vivo and in vitro experiments, minimum 3 biological replicates and minimum 2 independent experiments were performed. Samples size and number of independent experiments are indicated in the figure legends.
Data exclusions	No data were excluded from the analysis.
Replication	All experiments were performed in 2-3 independent replicates. scRNA-Seq analysis was explorative and key genes were validated by FACS in 2-3 independent replicate experiments.
Randomization	Randomization was not relevant to this study. Mice were grouped by genotype/treatment and treated equally.
Blinding	No blinding was performed as mice were grouped by genotype/and all individual mice were treated equally.

Reporting for specific materials, systems and methods

We require information from authors about some types of materials, experimental systems and methods used in many studies. Here, indicate whether each material, system or method listed is relevant to your study. If you are not sure if a list item applies to your research, read the appropriate section before selecting a response.

Materials & experimental systems

n/a	Involved in the study
☐	☒ Antibodies
☐	☒ Eukaryotic cell lines
☒	☐ Palaeontology and archaeology
☐	☒ Animals and other organisms
☒	☐ Human research participants
☒	☐ Clinical data
☒	☐ Dual use research of concern

Methods

n/a	Involved in the study
☒	☐ ChIP-seq
☐	☒ Flow cytometry
☒	☐ MRI-based neuroimaging

Antibodies

Antibodies used

CD3ε Biotin Clone 145-2C11 BioLegend # 100304, 1:200
CD3ε BV421 Clone 145-2C11 BioLegend # 100341, 1:200
CD3g unconjugated Clone EPR4517 Abcam # ab134096, 1:4000
CD5 Biotin Clone 53-7.3 BioLegend # 100604, 1:500
CD5 FITC Clone 53-7.3 BioLegend # 100605, 1:400
CD16/32 unconjugated Clone 2.4G2 BioXCell # BE0307, 1:300
CD19 Biotin Clone 6D5 BioLegend # 115504, 1:300
CD19 FITC Clone 1D3 BioLegend # 152404, 1:200
CD45 AF700 Clone 30-F11 BioLegend # 103128, 1:500
CD45 BV510 Clone Rat IgG2b, κ 30-F11 BioLegend #103138, 1:500
CD45.1 BV785 Clone A20 BioLegend # 110743, 1:500
CD45.2 AF700 Clone 104 BioLegend # 109822, 1:500
CD45.2 BUV563 Clone 104 (RUO) BD # 741273, 1:400
CD49a BV605 Clone Ha31/8 BD # 740375, 1:300
CD49a BV480 Clone Ha31/8 BD # 746244, 1:300
CD49a BUV805 Clone Ha31/8 BD # 741976, 1:300
CD49b (DX5) AF488 Clone DX5 BioLegend # 108913, 1:200
CD49b (DX5) APC Clone DX5 BioLegend # 108910, 1:200
CD49b (DX5) FITC Clone DX5 BioLegend # 108906, 1:200
CD49b (DX5) PerCP-eF710 Clone DX5 eBioscience # 46-5971-82, 1:200
CD127 / IL-7Ra APC Clone A7R34 BioLegend # 135012, 1:200
CD127 / IL-7Ra Biotin Clone A7R34 BioLegend # 135006, 1:200

CD127 / IL-7Ra Biotin Clone SB/199 BioLegend # 121103, 1:200
CD127 / IL-7Ra BUV737 Clone SB/199 BD # 612841, 1:200
CD127 / IL-7Ra BV421 Clone A7R34 BioLegend # 135027, 1:200
CD160 PE Clone 7H1 BioLegend # 143003, 1:200
CD200R (Ox2R) PE Clone OX-110 BioLegend # 123907, 1:200
c-kit (CD117) APC Clone 2B8 BioLegend # 105812, 1:200
c-kit (CD117) PE Clone 2B8 BioLegend # 105808, 1:300
c-kit (CD117) PE-Cy7 Clone 2B8 BioLegend # 105814, 1:300
CXCR6 (CD186) APC Clone SA051D1 Biolegend # 151106, 1:200
CXCR6 (CD186) PE-Dazzle 594 Clone SA051D1 Biolegend # 151116, 1:200
Embigin PE Clone G7.43.1 Invitrogen # 12-5839-80, 1:200
Eomes PerCP-eF710 Clone Dan11mag eBioscience # 46-4875-82, 1:300
F4/80 Biotin Clone Rat IgG2a, κ BioLegend # 123106, 1:300
F4/80 FITC Clone BM8 BioLegend # 123108, 1:200
FcεRIα Biotin Clone MAR-1 BioLegend # 134304, 1:300
FcεRIα FITc Clone MAR-1 BioLegend # 134306, 1:300
GATA3 PE Clone TWAJ ThermoFisher # 12-9966-42, 1:200
Granzyme A APC Clone 3G8.5 ebioscience # 17-5831-80, 1:4000
Granzyme A eF450 Clone 3G8.5 eBioscience # 48-5831-80, 1:3000
Granzyme A PE Clone 3G8.5 BioLegend # 149703, 1:5000
Granzyme B AF700 Clone GB11 BD # 561016, 1:400
Granzyme B FITC Clone GB11 BioLegend # 515403, 1:200
IFN-γ APC Clone XMG1.2 BioLegend # 505810, 1:500
IL-18Ra (CD218a) APC Clone P3TUNYA Invitrogen # 17-5183-82, 1:200
IL-18Rα (CD218a) PE Clone P3TUNYA Invitrogen # 12-5183-82, 1:300
IL-18Rα (CD218a) PE-Cy7 Clone P3TUNYA Thermo # 25-5183-82, 1:300
Ly6G Biotin Clone 1A8 BioLegend # 127604, 1:300
NK1.1 BUV661 Clone PK136 BD # 741477, 1:300
NK1.1 BV650 Clone PK136 Biolegend # 108736, 1:300
NK1.1 PE-Cy7 Clone PK136 BioLegend # 108714, 1:300
NKp46 PerCP-eF710 Clone 29A1.4 eBioscience # 46-3351-80, 1:200
NKp46 PE-Cy7 Clone 29A1.4 Biolegend #137618, 1:200
RORγt BV421 Clone Q31-378 (RUO) BD # 562894, 1:400
Tbet BV421 Clone 4B10 BioLegend # 644815, 1:300
TCF-1/TCF-7 AF488 Clone C63D9 Cell Signalling # 6444S, 1:200
TCF-1/TCF-7 AF594 Clone C63D9 Cell Signalling # 35972, 1:200
TCRβ Biotin Clone H57-597 BioLegend # 109204, 1:300
TCRβ FITC Clone H57-597 BioLegend # 109206, 1:200
TCRγδ Biotin Clone eBio-GL3 eBioscience # 13-5711-85, 1:300
TCRγδ FITC Clone GL3 BioLegend # 118106, 1:200
TER-119 (Ly-76) FITC Clone TER-119 BioLegend # 116206, 1:200
TER-119 (Ly-76) Biotin Clone TER-119 BioLegend # 116204, 1:300
Goat tdTomato polyclonal antibody unconjugated Clone MyBioSource.com # MBS448092, 1:1000
Donkey anti-Rabbit IgG (H+L) Highly Cross-Adsorbed Secondary Antibody AF plus 488 plus Clone Invitrogen # A32790, 1:5000
Chicken anti-rabbit IgG (H+L) AF594 Clone Thermo Fisher # A21442, 1:5000
Donkey anti-Goat IgG (H+L) Cross-Adsorbed Secondary Antibody AF594 Clone Invitrogen # A11058, 1:1000
Hashtag 1 TotalSeq™-A0301 Clone 30-F11 BioLegend # 155801, 1:300
Hashtag 2 TotalSeq™-A0302 Clone 30-F11 BioLegend # 155803, 1:300
CD11b Totalseq-A0014 Clone M1/70 BioLegend # 101265, 1:500
CD27 TotalSeq-A0191 Clone LG.3A10 BioLegend # 124235, 1:300
CD69 TotalSeq-A0197 Clone H1.2F3 BioLegend # 104546, 1:300
CD90.2 Total Seq-A0075 Clone 30-H12 BioLegend # 105345, 1:500
CD127 TotalSeq-A0198 Clone A7R34 BioLegend # 135045, 1:200
CD200R (OX2R) TotalSeq-A0807 Clone OX-110 BioLegend # 123913, 1:300
NKp46 TotalSeq-A0184 Clone 29A1.4 BioLegend # 137633, 1:200
anti-ARTC2 Nanobody Clone S+16a Biolegend #149802

Validation

All antibodies used are commercially available and have been validated by the manufacturers.

BioLegend:
https://www.biolegend.com/en-us/quality/quality-control
Specificity testing of 1-3 target cell types with either single- or multi-color analysis (including positive and negative cell types). Once specificity is confirmed, each new lot must perform with similar intensity to the in-date reference lot. Brightness (MFI) is evaluated from both positive and negative populations.
Each lot product is validated by QC testing with a series of titration dilutions.

Abcam:
https://www.abcam.com/cd3g-antibody-epr4517-ab134096.html?productWallTab=ShowAll

Cell Signalling:
https://www.cellsignal.de/products/antibody-conjugates/tcf1-tcf7-c63d9-rabbit-mab-alexa-fluor-594-conjugate/35972?site-search-type=Products&N=4294956287&Ntt=35972&fromPage=plp&_requestid=1371113
https://www.cellsignal.de/products/antibody-conjugates/tcf1-tcf7-c63d9-rabbit-mab-alexa-fluor-488-conjugate/6444?site-search-type=Products&N=4294956287&Ntt=6444s&fromPage=plp&_requestid=1371183

BD

https://regdocs.bd.com/regdocs/qcinfo?_ga=2.52507304.1015884254.1626790987-49964411.1626790986

eBioscience / Invitrogen / Thermo Fisher
https://www.thermofisher.com/antibody/product/Embigin-Antibody-clone-G7-43-1-Monoclonal/12-5839-80
https://www.thermofisher.com/antibody/product/EOMES-Antibody-clone-Dan11mag-Monoclonal/46-4875-82
https://www.thermofisher.com/antibody/product/Gata-3-Antibody-clone-TWAJ-Monoclonal/12-9966-42
https://www.thermofisher.com/antibody/product/Granzyme-A-Antibody-clone-GzA-3G8-5-Monoclonal/17-5831-80
https://www.thermofisher.com/antibody/product/Granzyme-A-Antibody-clone-GzA-3G8-5-Monoclonal/48-5831-82
https://www.thermofisher.com/antibody/product/CD218a-IL-18Ra-Antibody-clone-P3TUNYA-Monoclonal/17-5183-82
https://www.thermofisher.com/antibody/product/CD218a-IL-18Ra-Antibody-clone-P3TUNYA-Monoclonal/12-5183-82
https://www.thermofisher.com/antibody/product/CD218a-IL-18Ra-Antibody-clone-P3TUNYA-Monoclonal/25-5183-82
https://www.thermofisher.com/antibody/product/CD335-NKp46-Antibody-clone-29A1-4-Monoclonal/46-3351-82
https://www.thermofisher.com/antibody/product/TCR-gamma-delta-Antibody-clone-eBioGL3-GL-3-GL3-Monoclonal/13-5711-82
https://www.thermofisher.com/antibody/product/Donkey-anti-Rabbit-IgG-H-L-Highly-Cross-Adsorbed-Secondary-Antibody-Polyclonal/A32790
https://www.thermofisher.com/antibody/product/Chicken-anti-Rabbit-IgG-H-L-Cross-Adsorbed-Secondary-Antibody-Polyclonal/A-21442

MyBioSource
https://www.mybiosource.com/polyclonal-antibody/tdtomato/448092

Eukaryotic cell lines

Policy information about cell lines

Cell line source(s)	JM8A3.N (Ronald Naumann, MPI-CBG, Dresden); OP9-DL1, OP9, OP9-DL4, YAC1 (all cells were originally obtained from ATCC)
Authentication	Cell line was not authenticated.
Mycoplasma contamination	Cell line was not tested for mycoplasma contamination.
Commonly misidentified lines (See ICLAC register)	No commonly misidentified cell lines was used.

Animals and other organisms

Policy information about studies involving animals; ARRIVE guidelines recommended for reporting animal research

Laboratory animals	Male and female mice at 8-16 weeks of age were used. Strains: C57BL/6, CD45.1 (B6.SJL-Ptprca Pepcb/BoyJ), Rag1KO, Rag2-/-gc-/-, HobitTom/KO, HobitTom/WT, NKp46iCre, Eomesfl/fl, HobitKO, Flp deleter, UbiCreERT2, RORc-Cre, Rosa-eYFP, FoxP3DTR
Wild animals	The study did not involve wild animals.
Field-collected samples	The study did not involve samples collected from the field.
Ethics oversight	Lower Franconia Government and the national guidelines of the Netherlands

Note that full information on the approval of the study protocol must also be provided in the manuscript.

Flow Cytometry

Plots

Confirm that:

☒ The axis labels state the marker and fluorochrome used (e.g. CD4-FITC).

☒ The axis scales are clearly visible. Include numbers along axes only for bottom left plot of group (a 'group' is an analysis of identical markers).

☒ All plots are contour plots with outliers or pseudocolor plots.

☒ A numerical value for number of cells or percentage (with statistics) is provided.

Methodology

Sample preparation	Liver, salivary glands and kidneys were harvested, cut into small pieces and digested in DMEM with 10 mM Hepes, 20 ug/ml DNase I and 1 mg/ml Collagenase D at 37°C and 100 rpm for 40 min. Suspensions were passed through 100 um filters and lymphocytes enriched by 40%/80% percoll gradient (860 x g, 20 min, RT, no breaks). The interphase was washed with PBS and used for flow cytometric analysis or sorting. Small intestine was harvested, Peyer's patches were removed, the intestine cut open longitudinally and washed extensively with PBS to remove feces. After dissociation using HBSS (Sigma Aldrich) supplemented with 5 mM EDTA (Carl Roth) and 10 mM Hepes at 37°C, tissue were cut into small pieces and digested in HBSS with 10 mM Hepes, 20 Eg/ml DNase I, 0.5 mg/ml Collagenase D and 50 U/ml Dispase (Corning) at 37°C and 100 rpm for 1h. Suspensions were passed through 100 Em filters and lymphocytes enriched by 40%/80% percoll (Sigma Aldrich) gradient (860 x g, 20 min, RT, no breaks). The interface was

	washed with PBS (Sigma Aldrich) and used for flow cytometric analysis or sorting. Mesenteric lymph node cell suspensions were filtered through 70 Em filters and used for flow cytometric analysis.
Instrument	BD Celesta (3 laser: violet/blue/red) BD FACSAria III (3 laser: violet/blue/red) Cytek Aurora (5 laser: UV/violet/blue/yellow-green/red)
Software	FACSDiva v9 SpectroFlo v2.2.0.2
Cell population abundance	Post sorting quality control yielded greater than 97% purity.
Gating strategy	Samples were pre-gated for lymphocytes (FSC-A/SSC-A), singlets (based on SSC-A/SSC-W), live cells (LD marker negative). For sorting, ILC1 were gated as live CD45+Lin-CD3e-NK1.1+CD49b-CD49a+ cells and subsets sorted based on CD127 and cKit. For FACS analysis, ILC1 were gated as live CD45+Lin-NK1.1+Eomes-CD49a+ cells or CD45+Lin-NK1.1+CD49b-CD49a+ cells. NK cells were gated as live CD45+Lin-NK1.1+Eomes+ cells or CD45+Lin-NK1.1+CD49b+ (CD49a-) cells. Small intestinal ILC1 were generally gated as live CD45+LinENKp46+NK1.1+Eomes-RORgt- cells or, to preserve the Hobit reporter signal, as live CD45+Lin-NKp46+NK1.1+CD90intCD127+CXCR6+ cells

☒ Tick this box to confirm that a figure exemplifying the gating strategy is provided in the Supplementary Information.